

# Recent Progress of Optoelectronic and All-Optical Neuromorphic Devices: A Comprehensive Review of Device Structures, Materials, and Applications

Seungho Song, Jeehoon Kim, Sung Min Kwon, Jeong-Wan Jo, Sung Kyu Park,\*  
and Yong-Hoon Kim\*

Conventional von Neumann-based computing systems have inherent limitations such as high hardware complexity, relatively inferior energy efficiency, and low bandwidth. As an alternative, neuromorphic computation is emerging as a platform for next-generation artificial intelligence computing systems due to their potential advantages such as highly energy-efficient computing, robust learning, fault tolerance, and parallel processing. Moreover, to further enhance the energy efficiency and processing speed, photonic-based neuromorphic systems have gathered significant interest in the past few years. Herein, the recent progress and development of optoelectronic and all-optical neuromorphic devices is summarized, focusing on their structures, materials, and potential applications. Particularly, for optoelectronic neuromorphic devices, devices with planar and vertical structures are described along with their key strategies in materials and device structures. Next, all-optical memory and neuromorphic devices for neuromorphic computing are reviewed. Finally, the applications of optoelectronic neuromorphic devices are discussed for their potential utilization in neuromorphic computing systems.

## 1. Introduction

Current computation systems are generally based on the von Neumann architecture.<sup>[1,2]</sup> However, despite the significant efforts to overcome the limitations of von Neumann-based computation, high-speed and energy-efficient operation is still limited mainly due to the physical separation between processing and memory units as well as the serial processing architecture. To resolve this issue, particularly to overcome the limitations of von Neumann-based computation, neuromorphic computing systems have been intensively researched over the last decade.<sup>[3,4]</sup> One of the main objectives of the next-generation computation systems is mimicking the human brain, particularly its complex functions and structures, which may enable energy-efficient computation

and massive parallel processing. In a human brain, the neural network, which consists of large numbers of neurons and synapses, is considered to be the key element for performing complex behaviors such as synaptic plasticity, short-term memory (STM)/long-term memory (LTM), spike timing-dependent plasticity (STDP), and paired pulse facilitation (PPF).<sup>[5]</sup> For example, synaptic plasticity, in which the connection strength between the neurons relies on the characteristics of the stimuli, is considered one of the most important neural functions. Also, the STM/LTM functions are related to the memorization function of the brain. In the case of STM, which is believed to be stored in the hippocampus,<sup>[6]</sup> a memory can only persist for a short period of time, and the memory is lost rapidly when the stimuli is removed. On the other hand, in the case of LTM, which occurs by repetitive and frequent input stimuli to the brain, a memory is stored for a relatively longer period of time compared to the STM. Furthermore, STDP is also an essential function of the neural network. The STDP refers to the change of synaptic connection (or strength) between the presynaptic and postsynaptic neurons. Depending on the timing of the spikes occurring between the presynaptic and postsynaptic neurons, their connection strength can be varied.<sup>[7,8]</sup> It is reported that there are several types of STDP behaviors occurring in the brain, such as symmetric and asymmetric STDP.<sup>[9]</sup> In addition, PPF is a type of neural facilitation similar to short-term synaptic plasticity where the

S. Song, J. Kim, Prof. Y.-H. Kim  
School of Advanced Materials Science and Engineering  
Sungkyunkwan University  
Suwon 16419, Korea  
E-mail: yhkim76@skku.edu

S. M. Kwon, Prof. S. K. Park  
School of Electrical and Electronics Engineering  
Chung-Ang University  
Seoul 06980, Korea  
E-mail: skpark@cau.ac.kr

Dr. J.-W. Jo  
Electrical Engineering Division  
Department of Engineering  
University of Cambridge  
Cambridge CB3 0FA, UK

Prof. Y.-H. Kim  
SKKU Advanced Institute of Nanotechnology (SAINT)  
Sungkyunkwan University  
Suwon 16419, Korea

 The ORCID identification number(s) for the author(s) of this article can be found under <https://doi.org/10.1002/aisy.202000119>.

© 2020 The Authors. Published by Wiley-VCH GmbH. This is an open access article under the terms of the Creative Commons Attribution License, which permits use, distribution and reproduction in any medium, provided the original work is properly cited.

DOI: 10.1002/aisy.202000119

postsynaptic potentials increased by an impulse are affected by the prior impulse.

To realize neuromorphic computing systems that can mimic various neural functions, diverse artificial neuromorphic devices have been investigated. For instance, for a neuromorphic device, devices such as memristors,<sup>[10]</sup> atomic switches,<sup>[11,12]</sup> transistors,<sup>[13–15]</sup> and memtransistors<sup>[16,17]</sup> have been widely investigated. As a result, various important functions of the neural network could be mimicked. More recently, to further enhance the energy efficiency and to potentially increase the operation speed of the neuromorphic computing systems, optoelectronic and all-optical neuromorphic devices have been actively researched.<sup>[18–22]</sup> In the case of electrical neuromorphic devices, the computational speed can be inevitably limited mainly due to the bandwidth–connection–density trade-off.<sup>[23]</sup> However, in optoelectronic and all-optical neuromorphic devices, using light as the stimulation source instead of electrical pulses, high-speed, high-bandwidth, low-crosstalk, and more energy-efficient neuromorphic systems could be realized.<sup>[24,25]</sup> Particularly, the energy consumption can be comparably lower (approximately subpicojoule) than that of electrical neuromorphic devices (sub- to a few nanojoules).<sup>[26–29]</sup> Also, the bandwidth can be drastically enhanced up to 200 GHz by implementing the light source as a main input that is higher than the bandwidth of the conventional electronics (approximately subgigahertz).<sup>[30]</sup> Moreover, studies have shown that the photonic-based architecture can tolerate a large portion of device faults, around 20%,<sup>[31]</sup> which the conventional architecture is not able to do. Previously, Xu et al. reported the comparison of computation time for photonic computing systems with the existing central processing units (CPUs), graphics processing units (GPUs), and supercomputers.<sup>[32]</sup> Although the computation time of photonic computing systems was slightly increased as the problem size increased, the CPU, GPU, and supercomputers showed a linear increase of computation time with the problem size. Moreover, the photons in waveguides have extremely high speed ( $\approx 2 \times 10^{11}$  mm s<sup>-1</sup>), which may also increase the data transport in photonic-based computing systems.<sup>[32]</sup> Sun et al. also reported a *state-of-the-art* roadmap using silicon photonic and electronic systems.<sup>[33]</sup> Here, it is argued that the energy efficiency of the silicon photonics can outperform the conventional electronics, and it is expected that the energy efficiency could be reduced down to pico- to femtojoules which, the conventional electronics can hardly reach. In addition, by integrating optical waveguides and multiwavelength light sources at a chip level, multiplexed computation could be possible, enabling the realization of high-speed optoelectronic or all-optical neuromorphic chips.<sup>[34]</sup>

Due to these potential advantages of optoelectronic and all-optical neuromorphic devices, many innovative devices have been demonstrated using materials such as 1D carbon nanotubes (CNTs),<sup>[35,36]</sup> 2D MoS<sub>2</sub>,<sup>[37,38]</sup> black phosphorus (BP),<sup>[39]</sup> graphene,<sup>[40]</sup> graphene oxides (GOs),<sup>[41]</sup> metal oxides,<sup>[18,42–46]</sup> organics,<sup>[47]</sup> and halide perovskites.<sup>[48]</sup> Using these devices and their integrated circuits, various synaptic and neuromorphic functions, such as STM/LTM, STDP, and PPF, have been successfully mimicked. In addition, artificial optical nerves, motor nerve systems, and the emulation of Pavlov's dog behavior were also demonstrated.<sup>[49–51]</sup>

One of the major differences between the optoelectronic and electrical neuromorphic devices is the stimulation source. In optoelectronic neuromorphic devices, optical signals are used to stimulate the device and change its weight (or conductance), whereas in electrical neuromorphic devices, voltage pulses are used as the stimulation. Despite the difference in the stimulation source, however, the algorithms used to perform the neuromorphic functions in electrical neuromorphic devices can be also used for the optoelectronic neuromorphic devices. For instance, handwritten pattern recognition is one of the representative applications of the neuromorphic algorithms. Whether the input is an optical signal or an electrical signal, the methods of applying the neuromorphic algorithms are ideally the same. As an example, Hu et al. implemented a single-layer-perceptron-based artificial neural network learning algorithm for an optoelectronic memristive device to demonstrate pattern recognition of handwritten patterns,<sup>[47]</sup> and it was shown that the device exhibited a relatively high recognition rate comparable with that of conventional electrical memristors.<sup>[52]</sup>

In previous studies on optoelectronic neuromorphic devices, several different types of device structures and materials have been suggested. Particularly, two- and three-terminal planar structure devices and two-terminal vertical structures have been widely investigated. The planar structure devices have advantages such as simple device structure and fabrication process because their structures are very similar to those of conventional phototransistors.<sup>[53–55]</sup> Meanwhile, the vertical structure devices have advantages such as small device size and low operation voltage, which can allow high-density integration and higher energy efficiency, respectively. This review provides an overview of the optoelectronic and all-optical neuromorphic devices, focusing on their device structures, materials, and applications. Particularly, for optoelectronic neuromorphic devices, planar and vertical structure devices are described, including their operation mechanisms and neuromorphic applications. Furthermore, all-optical memory and neuromorphic devices are also reviewed, concerning their device structure and materials. Finally, the applications of optoelectronic neuromorphic devices and integrated circuits are reviewed to envision the potential utilization for neuromorphic electronics.

## 2. Optoelectronic Neuromorphic Devices

### 2.1. Materials for Optoelectronic Neuromorphic Devices

For optoelectronic neuromorphic devices, various materials, including organics, metal oxides, low-dimensional materials, and perovskite materials, have been studied, as listed in **Table 1**. The organic semiconductor materials have advantages such as low-temperature processing, simple solution processing, and a wide variety of material candidates. Also, the organic materials are mechanically flexible, and thus, organic materials can be attractive choices when neuromorphic devices are fabricated on a flexible substrate.<sup>[56]</sup> More importantly, the optical and electrical properties of organic materials can be modified by a molecular design; therefore, fine-tuning of optical and electrical properties

**Table 1.** Device structure, active material, dimensions, operation conditions, and energy consumption of vertical/planar structure optoelectronic neuromorphic devices and all-optical neuromorphic devices.

Material (active layer)	Structure	Scale	Light pulse intensity	Light pulse width	Electrical bias	Energy consumption	Ref.
WS <sub>2</sub>	Planar	Few tens of μm	0.19–28 μW	100 ms	0.1, 5 V (gate)	–	[16]
IGZO	Planar	–	0.6 mW cm <sup>-2</sup>	500 ms	10 V	–	[18]
WSe <sub>2</sub>	Planar	5 μm	6 mW cm <sup>-2</sup>	10 ms	0.3 V	66–532 fJ	[26]
SWNT	Planar	100 nm <sup>2</sup>	40 W cm <sup>-2</sup>	Few seconds	2, 3.5 V	–	[35]
HfO <sub>2</sub>	Planar	200 μm × 1000 μm	0.025 mW	–	–	–	[36]
MoS <sub>2</sub>	Planar	15 μm × 10 μm	50 mW cm <sup>-2</sup>	100 ms	1, 2–3 V	80 pJ per spike	[37]
MoS <sub>2</sub>	Planar	few tens of μm	5.45 mW	2, 3 s (interval)	4, 2 V	–	[38]
Graphene	Planar	90 μm × 30 μm (width, length)	50–200 μW	5, 0.1 ms	10–40 V (gate)	–	[40]
IGZO	Planar	10 μm <sup>2</sup>	100 μW	50 ms	1–4 V	150–pJ	[41]
IGZO	Planar	800 μm × 500 μm	15–120 μW cm <sup>-2</sup>	2 s	0.1–20 V	≈ 1 nW	[42]
LaSrNiO <sub>4</sub>	Planar	–	220 mW cm <sup>-2</sup>	5, 10 s	–	–	[43]
CuPc	Planar	1000 and 100 μm	0.13–1.27 mW cm <sup>-2</sup>	0.5 s	5–10 V	–	[47]
IGZO	Planar	700 × 900 μm <sup>2</sup>	22 mW cm <sup>-2</sup>	0.5 s	1 V (Bias), 2 V (spike), 3 V	–	[49]
Solid electrolyte (SE)	Planar	100–200 μm	7 μW cm <sup>-2</sup>	10 ms	1.5 mV	2.41 pJ	[50]
CdS	Planar	–	10 mW cm <sup>-2</sup>	500 ms	10 V	–	[51]
CH <sub>3</sub> NH <sub>3</sub> PbI <sub>3</sub>	Planar	–	≈ 1.29 μW cm <sup>-2</sup>	–	1 V (10 ms)	–	[74]
CsPbBr <sub>3</sub> (QD)	Planar	50, 1000 μm	0.153 mW cm <sup>-3</sup>	1 s	10 V	1.4 nJ per event	[75]
C8-BTBT	Planar	40, 20 μm (width, length)	0.32, 16 (mainly), 40 mW cm <sup>-2</sup>	500 ms	–2 V	≈ 13.6 pJ	[76]
MAPbI <sub>3</sub>	Planar	25 μm × 500 μm (Channel)	1 μW cm <sup>-2</sup>	200 ms	0.01 V (bias), 1–4 V (gate)	1 pJ	[77]
DPPDTT	Planar	30 μm, 1 mm (Length, Width)	0.06–1.20 mW cm <sup>-2</sup>	0.6 s	–1 to –4 (bias), –0.2, –3 (gate voltage)	0.5 fJ (at 0.0005 V, 50 ms)	[78]
Methylammonium lead bromide PQDs	Planar	15 μm (channel length)	190 nW cm <sup>2</sup> ≈ 1.1 μW cm <sup>2</sup>	Few seconds	0.5 V, 5 s (bias), 0–100 V (gate), mainly 10, 0.5 V 1 s (pulse)	36.75 pJ per spike (graphene)	[79]
Sol-PDI, BPE-PDI	Planar	50, 1000 μm	8–10 mW cm <sup>2</sup>	<3 s (programming time)	1.0, 0.1 V (programming), 60 V (erasing, few seconds)	–	[80]
Dif-TES-ADT/ BCB	Planar	–	5 μW cm <sup>-2</sup>	30–180 ms	5 V (gate)	–	[81]
C8-BTBT/ PAN	Planar	30 μm	0.16–0.90 mW cm <sup>-2</sup>	100–500 ms	2 V (gate)	–	[82]
Silver nanowires	Planar	≈ 0.6 cm <sup>2</sup>	4 mW cm <sup>-2</sup>	1–10 s	≈ 0.6 V	≈ 4 μJ	[111]
BP	Planar	9.2 ± 1.1 μm <sup>2</sup>	3–10 mW cm <sup>-2</sup>	100 ms	10 mV	9.24 × 10 <sup>2</sup> pJ (electrical), 3.5 pJ (optical) per synaptic activity	[112]
MoS <sub>2</sub>	Planar	–	5.25 mW mm <sup>-2</sup>	10 s	1–2 V	–	[113]
MoO <sub>x</sub>	Vertical	Diameter of ITO 250 μm	0.22, 0.45, 0.65, 0.88 mW cm <sup>-2</sup>	200 ms	–3 to 3 V, –4.5 V (erase)	–	[21]
Nb:SrTiO <sub>3</sub>	Vertical	Diameter of ITO 400 μm	30 mW cm <sup>-2</sup>	–	0.05 V (read)	–	[22]
CeO <sub>2-x</sub>	Vertical	Diameter of 100 μm	60 pW μm <sup>-2</sup>	4 s	0.2 V (read), –2, 10 V (pulse)	600 pW	[45]
CeO <sub>2-x</sub>	Vertical	200 μm	6 pW μm <sup>-2</sup>	3 s	–2 to 2 V, –2 (erase)	–	[46]
CH <sub>3</sub> NH <sub>3</sub> PbI <sub>3</sub>	Vertical	Diameter of Ag 100 μm	10 mW cm <sup>-2</sup>	300 ms	0.05–0.3 V	–	[48]
BiFeO <sub>3</sub> /SrRuO <sub>3</sub>	Vertical	–	10 m W cm <sup>-2</sup>	500 μs	–2 V (read), –6 (write)	≈ 0.2 nJ	[72]
MoS <sub>2</sub>	Vertical	Diameter of W 50 μm	0.11 mW cm <sup>-2</sup>	1 s (photonic), 5 ms (electronic)	0.1 V (read)	–	[83]

**Table 1.** Continued.

Material (active layer)	Structure	Scale	Light pulse intensity	Light pulse width	Electrical bias	Energy consumption	Ref.
InO <sub>2</sub> /ZnO	Vertical	–	0.4 mW cm <sup>-2</sup> , 4 mW cm <sup>-2</sup>	20 ms	–2 to 2 V, –1 V (erase)	0.7 pJ	[84]
MAPbI <sub>3</sub>	Vertical	diameter of ITO 7 μm	50 μW cm <sup>-2</sup>	5 ns	–1 to 1 V	–	[85]
Nb:STO	Vertical	–	2.5 mW cm <sup>-2</sup>	5 ms	–2 to 2 V, –8 V, –4 V (erase), 1.4 V (write)	–	[86]
EGaIn/poly-L-histidine/ Au nanorod	Vertical	–	0.03 W cm <sup>-2</sup>	5 s	2.5 V	–	[87]
ZnO <sub>1-x</sub>	Vertical	A diameter of 100 μm	0.005–0.072 mW cm <sup>-2</sup>	1 s	0.1, 4 V	–	[88]
PMMA	Vertical	500 μm	0.05 mW cm <sup>2</sup>	0.1 s	5 V	–	[89]
GO	Vertical/ Planar	50 μm	44 mW cm <sup>-2</sup>	60–1800 s	0.1 V, 0.68 < V < 0.82	–	[90]
MXene	Vertical	5 mm <sup>2</sup>	0.65 ± 0.06 mW mm <sup>-2</sup>	0.5 ms	3 V	–	[109]
GST	Waveguide	1 × 3 μm <sup>2</sup>	1 W	50 ns	–	243 pJ	[20]
GST	Waveguide	0.25 μm <sup>2</sup>	150 mW	10–20 ns	–	480 fJ	[91]
GST	Waveguide	1500 μm × 300 μm (width, length)	–	200 ns	–	710 pJ	[92]

could be also possible.<sup>[57–59]</sup> However, it should be considered that the organic materials are relatively unstable compared to inorganic materials due to problems such as oxidation. To improve the stability of the organic materials, hybridization with various materials has been actively researched recently.<sup>[60,61]</sup> Oxide materials, especially metal oxide semiconductors, have advantages such as high carrier mobility, high stability, good transparency, and decent mechanical flexibility.<sup>[62]</sup> Moreover, the oxygen vacancies that exist in oxide semiconductors can be ionized under light illumination, providing a pathway to control the conductivity of the semiconductor. Due to these characteristics, oxide semiconductors can be utilized for active layers in various optoelectronic neuromorphic devices.<sup>[63,64]</sup>

Perovskite materials are known as excellent photoelectric conversion materials. Particularly, organic perovskite materials have been intensively researched for photovoltaic devices, such as solar cells.<sup>[65,66]</sup> Also, perovskite materials can be used for various photosensing elements. However, perovskite materials also have some instability issues similar to the organic materials. To improve the stability, inorganic–organic hybrid materials and inorganic perovskite materials have been investigated.<sup>[66]</sup> Nevertheless, due to these optical/electrical characteristics of perovskite materials, they are receiving great attention in the optoelectronics field. In addition, low-dimensional 1D (nanowires, nanotubes, etc.) and 2D materials have unique optoelectronic properties compared to their bulk counterparts. Originating from their restricted dimensions, 1D materials typically show improved charge transport and exciton confinement.<sup>[67,68]</sup> Also, 2D materials could exhibit high photosensitivity even with an extremely thin layer (atomic level). In addition, the trap sites that exist in 2D materials can be utilized for optoelectronic synapse devices that operate based on the charge trapping mechanism.<sup>[69,70]</sup> Furthermore, due to the extremely thin thickness of the low-dimensional materials, they tend to have great mechanical flexibility.

## 2.2. Planar Structure Devices

For optoelectronic neuromorphic devices, planar structure devices have been most widely adopted due to their simple device structure. In planar structure devices, the electrodes are placed on the same plane as a two-terminal device. Also, an additional gating electrode can be added as a third electrode, which is typically used to modulate the carrier concentration and the light-response characteristics. However, as described, the planar structure devices have a limitation for down-scaling. Also, adding an additional gating electrode could complicate the circuit design as well as their operation scheme. Despite these disadvantages, planar structure optoelectronic devices have been intensively studied for neuromorphic applications because of their easy device design and process compared to other types of devices.

### 2.2.1. Metal-Oxide-Based Devices

Previously, Yu et al. reported optoelectronic synapse devices using SnO<sub>x</sub>/poly(3,4-ethylenedioxythiophene) polystyrene sulfonate (PEDOT:PSS) layers placed on top of an indium gallium zinc oxide (IGZO) layer with low power consumption (≈10 pW). Here, to operate the device, a light pulse with a pulse width of 2 s and power intensity of 15–120 μW cm<sup>-2</sup> was used. Also, an electrical bias in the range of 0.1–20 V was used to modify the amplitude of photocurrent change. In this device, the synaptic functions could be emulated by the persistence photoconductivity (PPC) behavior of the oxide semiconductor. The PPC behavior is a phenomenon in which the conductivity level decays back to its original state slowly even after the light is turned off. It is claimed the PPC behavior in oxide semiconductors is related to the two types of defect states, namely, the α-type (nonconducting defect-localized states) and β-type (defects that can provide electrons to the conduction band minimum) defects.<sup>[42]</sup> In fact, the oxygen vacancies, which are the point

defects where the oxygen atoms are missing from their lattice sites, can be  $\alpha$ - ( $V_O^0$ ) or  $\beta$ -type ( $V_O^{1+}$ ,  $V_O^{2+}$ ) defects depending on their charged states. By the light illumination, the neutral oxygen vacancy can be ionized, providing excess electrons to the bulk, increasing the conductivity of the film. Because activation energy is required to neutralize the ionized oxygen vacancies back into the neutral state, slow decaying of conductivity is typically observed in oxide semiconductors. In addition, it is claimed that the  $\text{SnO}_x$  placed on the IGZO layer can extract weakly bound oxygen atoms from IGZO, creating more oxygen vacancies. Furthermore, the p-type PEDOT:PSS can suppress the recombination of photogenerated electron-hole pairs (EHPs), leading to an increment of the conductivity. It has been shown that the device consumes less than 9 pW and uses less than 40 pJ energy when stimulated with a light source having power intensity of  $15 \mu\text{W cm}^{-2}$ . Lee et al. also demonstrated optoelectronic synapse devices using amorphous oxide semiconductors (AOSs)

mimicking brain-like behaviors such as STM/LTM, STDP and neural facilitation.<sup>[18]</sup> Due to the inherent PPC behavior of AOSs, various synaptic functions could be emulated. **Figure 1a** shows the schematic device structure of the IGZO-based optoelectronic synaptic device. When UV light ( $\lambda = 380\text{--}385 \text{ nm}$ ) is applied, the IGZO showed an increase in conductivity and due to the strong PPC behavior of IGZO, the conductivity persists even after the light is turned off. The emulation of STM and LTM behaviors is shown in Figure 1b,c, respectively. When a light stimulus with a low frequency of 0.2 Hz is applied to the device (intensity of  $0.6 \text{ mW cm}^{-2}$  and pulse width of 0.5 s), the device exhibited STM-like behavior, while light stimuli with a high frequency of 1 Hz induced LTM-like behavior.

Zhao et al. reported memcapacitor-based synapse devices using an  $\text{Au/La}_{1.875}\text{Sr}_{0.125}\text{NiO}_4$  (LSNO)/Au structure. Here, the capacitance of the device was modulated by optical and electrical stimulations.<sup>[43]</sup> Particularly, when UV light ( $\lambda = 365 \text{ nm}$ )

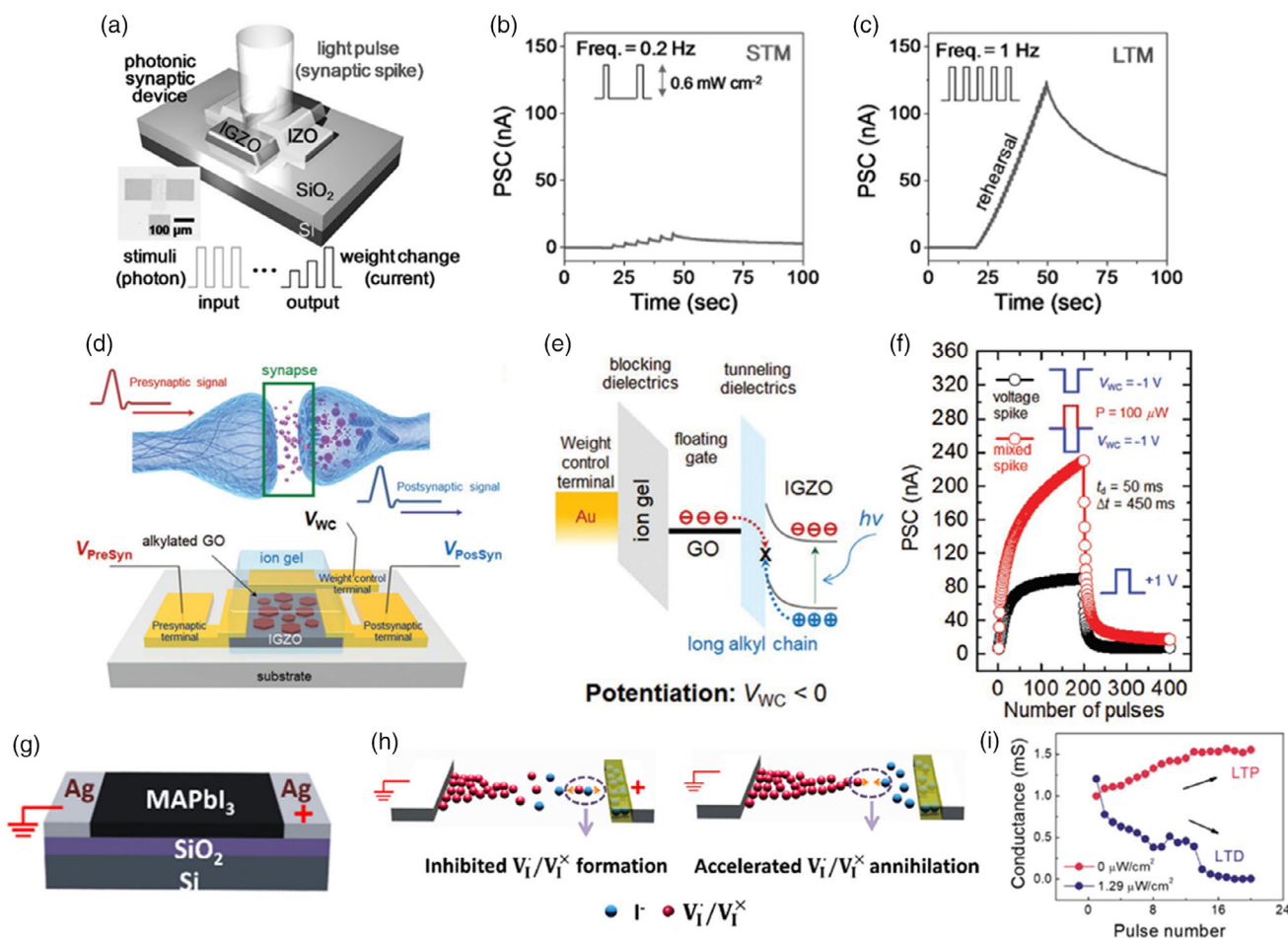


**Figure 1.** a) The device structure and an optical image of a planar structure IGZO-based optoelectronic neuromorphic device. The emulation of b) STM and c) LTM behaviors using different frequencies of light stimuli. (a–c) Reproduced with permission.<sup>[18]</sup> Copyright 2017, Wiley-VCH. d) An illustration of a biological synapse (top) and the device structure of an alkylated GO-based synaptic transistor (bottom). e) An energy band diagram describing the tunneling mechanism under light stimulation. f) Comparison of LTP/LTD characteristics with voltage spike (black) and mixed spike (red). (d–f) Reproduced with permission.<sup>[41]</sup> Copyright 2018, Wiley-VCH. g) The device structure of a planar-type  $\text{MAPbI}_3$ -based memristive device. h) Schematics describing the inhibition of iodine vacancy formation and the acceleration of iodine vacancy annihilation. i) The conductance variation of the device as a function of input pulses with and without light illumination. (g–i) Reproduced with permission.<sup>[74]</sup> Copyright 2018, American Chemical Society.

with an intensity of  $220 \text{ mW cm}^{-2}$  is irradiated, the initially trapped holes are detrapped, resulting in the formation of empty negatively charged traps that can reduce the depletion width and the Schottky barrier height.<sup>[71]</sup> Here, the Schottky barrier height represents the energy barrier formed at the metal–semiconductor contact interface. On the other hand, when the light is turned off, the holes can be recaptured, resulting in an increase of the Schottky barrier height. It was reported that the energy consumption was  $9 \times 10^4$ – $2.25 \times 10^6$  nJ with the light intensity of  $20$ – $250 \text{ mW cm}^{-2}$ . Using the device, synaptic functions such as STM/LTM, photonic potentiation/electric depression, and PPF are emulated, which are crucial characteristics for realizing applications of artificial electronic eyes and photonic neuromorphic computing systems. Another work using an IGZO semiconductor was demonstrated by Sun et al., where a GO charge-trapping layer was inserted to modulate the synaptic plasticity.<sup>[41]</sup> A schematic device structure of the synaptic transistor with alkylated GO is shown in Figure 1d. Here, single nanosheet alkylated GOs are embedded between the IGZO channel and the ion-gel dielectric layers. For the stimulation, a light pulse with pulse width of 50 ms and power intensity of  $100$ – $2000 \mu\text{W}$  was used. Also, an electrical pulse having an amplitude of 1 V and pulse width of 50 ms was used. The total energy consumption (electrical and optical energy) was  $\approx 10$  nJ with a device dimension of  $10 \times 10 \mu\text{m}^2$ , which is a reasonable value considering the device size. Figure 1e shows the energy band diagram describing the mechanism under light stimulation. When light is irradiated on the device, the IGZO light-responsive layer generates EHPs with the assistance of an electric field. The photoinduced holes from the IGZO induce detrapping of electrons from the GO nanosheet, causing a large increase in conductance. To emulate the long-term potentiation (LTP) and long-term depression (LTD)-like behaviors, mixed spikes of electrical and optical stimuli were applied to the device, as shown in Figure 1f. Compared to the case when only electrical stimulation is applied, the postsynaptic current (PSC) is increased in all regions when light is additionally applied.

Ferroelectric oxide materials can also play an important role in optoelectronic neuromorphic devices due to their long carrier lifetime.<sup>[16,44,72]</sup> Kim et al. reported synapse devices using ferroelectric  $\text{HfZrO}_x$  as an active layer to emulate synaptic behaviors such as short-term plasticity (STP), PPF, and LTP with light stimulation.<sup>[44]</sup> When the ferroelectric  $\text{HfZrO}_x$  is in downward polarization state after applying a bias of  $-5$  V (pulsed width of 10 ms), the electrons generated by the light (power intensity of  $10 \text{ mW cm}^{-2}$ ) are inhibited from recombining with the holes, whereas with upward polarization state, induced by applying a bias of 5 V (pulsed width of 10 ms) to the gate electrode, the recombination can be accelerated due to the band bending.<sup>[44]</sup> It is shown that conductance amplification of  $\approx 280\%$  and  $200\%$  was observed when the device had downward and upward polarization, respectively.

### 2.2.2. 1D and 2D Material-Based Devices

1D CNTs can be also used in memory and neuromorphic devices. Recently, Agnus et al. reported poly(3-octylthiophene-2,5-diyl)/single-walled carbon nanotube (SWNT)-based planar

structure transistor-type nonvolatile memory devices operated by light.<sup>[35]</sup> In these devices, the conductivity is increased by light illumination and the increased conductivity can be maintained by the trapping and accumulation of photogenerated electrons at the SWNT/dielectric interface. Here, a light source having a wavelength ( $\lambda$ ) of 457 nm and power intensity of  $40 \text{ W cm}^{-2}$  was used, and for the programming, electrical biases of  $0.4$ – $2$  and  $2$ – $6$  V for source-drain voltage and source-gate voltage were used, respectively.<sup>[35]</sup> In this work, four synapse devices were parallelly attached and the conductance variations caused by the photogating effect and electric field were summed at the neuron part. The results demonstrated the potentials of programmable integrated nonvolatile optoelectronic synaptic devices without a crosstalk. In addition, Shao et al. reported three-terminal planar structure synapse devices with printed SWNTs.<sup>[36]</sup> Due to the photogating effect, the photogenerated holes are trapped in the channel layer under light illumination and when the number of trapped holes exceeds the number of released holes, the current is increased. Here, the variation of synaptic plasticity was investigated depending on the wavelength, illumination time, and power of the light stimulation. Particularly, a light pulse having power of  $0.025$ – $2.17 \text{ mW}$  and pulse frequency of  $0.5$ – $10$  Hz was used. Also, light sources with different wavelengths were used (520, 940, and 1310 nm). Qin et al. also reported a three-terminal planar structure optoelectronic synapse device using a SWNT/graphene heterostructure.<sup>[40]</sup> Here, the channel size of the device was  $30 \times 90 \mu\text{m}^2$ , and for the stimulation, a light pulse having power intensity of  $10$ – $300 \mu\text{W}$  and pulse width of 5 ms was used (interval of 10 ms). Also, a gate bias of  $10$ – $40$  V was applied during the operation. When a negative gate field is applied to the device, photogenerated holes that were present in the graphene and SWNTs are trapped at the trap sites. Due to the high trap energy barrier, long photogating effect could be induced.<sup>[40]</sup> Using these phenomena, an axon multisynapse network was mimicked by stimulating two presynapses with a variation of spike timing difference for spatiotemporal amplitude summation. In addition, basic logic operations such as the NOR gate were also demonstrated.<sup>[40]</sup>

In addition to 1D materials, 2D materials also have attracted much attention in neuromorphic devices. For example, BP is a promising 2D material candidate due to its direct bandgap even in the bulk state. Ahmed et al. reported planar structure optoelectronic synapse devices using oxidized BPs.<sup>[39]</sup> In this work, the BP-based synapse devices were fabricated using exfoliated BPs from a bulk crystal. They demonstrated digital logic operations using the BP synapse devices, controlled by light stimuli. Wang et al. reported optoelectronic neuromorphic devices using a  $\text{MoS}_2$ /hexagonal boron nitride heterostructure.<sup>[37]</sup> The device had channel width and length of 10 and  $15 \mu\text{m}$ , respectively. Basic synaptic plasticity was emulated by utilizing the interfacial effect occurring at the  $\text{MoS}_2/\text{AlO}_x$  dielectric interface. In this device, the inhibition behavior was triggered by electrical pulses, while the potentiation was triggered by using both electrical and optical stimulations. For potentiation, a light pulse having power intensity of  $50 \text{ mW cm}^{-2}$  and pulse width of 100 ms was used ( $\lambda = 473, 532, \text{ and } 655 \text{ nm}$ ). For inhibition, an electrical pulse with pulse width of 50 ms and amplitude of 3 V was applied to the back gate. The power consumption for a single spike was 80 pJ. Zhang et al. also reported planar structure synaptic

devices consisting of a MoS<sub>2</sub> channel and high-*k* Ta<sub>2</sub>O<sub>5</sub>-TiO<sub>2</sub> (TTO) sandwiched between Al<sub>2</sub>O<sub>3</sub> dielectric layers for a charge-trapping layer.<sup>[38]</sup> Here, the photogenerated carriers can tunnel through the Al<sub>2</sub>O<sub>3</sub> layer and into the TTO layer by the Fowler–Nordheim tunneling mechanism, in which the electrons tunnel through a rounded triangular barrier created near the electrode surface by a substantially high electric field.<sup>[73]</sup> The trapped electrons in the TTO layer then block the back-gate electric field, allowing the electrons to transfer to the MoS<sub>2</sub> channel layer. With a reverse bias, the holes can be trapped in a similar way to create a different memory state. For the light stimulation, a light pulse with power intensity of 4.45 mW or 5.45 mW and pulse width of 2 s was used ( $\lambda = 520$  nm) using laser sources. Also, an electrical pulse with amplitude of 1–2 V, and pulse width of 10 ms was used (interval of 10 s). Luo et al. reported artificial synapse devices using a planar structure WS<sub>2</sub>/PbZr<sub>0.2</sub>Ti<sub>0.8</sub>O<sub>3</sub> (PZT) active layer.<sup>[16]</sup> Here, the light illumination induced downward alignment of the PZT polarization, which can change the conductivity of WS<sub>2</sub>. By controlling the degree of polarization by optical and electrical stimulations, multilevel and volatile/nonvolatile synaptic memory characteristics could be obtained. Here, a light pulse having pulse width of 100 ms and power intensity of 0.19–28  $\mu$ W was applied. Also, an electrical bias of 0.1 V was applied to read out the data.

### 2.2.3. Perovskite-Based Devices

Zhu and Lu reported optogenetics-inspired and controllable synaptic functions using organic–inorganic halide perovskite-based memristors.<sup>[74]</sup> A schematic structure of the planar-type Ag/MAPbI<sub>3</sub>/Ag memristor device is shown in Figure 1g. Here, using light, the generation and annihilation dynamics of iodine vacancies ( $V_i/V_i^x$ , positively charged or neutral vacancies) could be controlled by changing the formation energy of an iodine vacancy ( $V_i/V_i^x$ ). Particularly, the light illumination increased the formation energy and delayed the growth of  $V_i/V_i^x$  abundant regions in the MAPbI<sub>3</sub> film (Figure 1h). Without the electrical bias, the light facilitated the recombination of  $V_i/V_i^x$  and I<sup>-</sup>. Due to the suppression of  $V_i/V_i^x$  formation under light illumination (intensity of 1.29  $\mu$ W cm<sup>-2</sup>), as shown in Figure 1i, LTD could be emulated. Also, the LTP was emulated with a low bias of 1 V, with a duration of 10 ms and an interval of 1 ms. Wang et al. also reported a three-terminal planar structure photonic flash memory utilizing inorganic perovskite quantum dots (PQDs).<sup>[75]</sup> The device consists of pentacene/poly(methyl methacrylate) (PMMA)/CsPbBr<sub>3</sub>, which is fabricated on a SiO<sub>2</sub>/Si substrate. It is claimed that the CsPbBr<sub>3</sub> inorganic PQDs are suitable for photonic flash memory devices because of the long carrier lifetime and high photoresponsivity. The channel had length and width of 1000 and 50  $\mu$ m, respectively. For potentiation, a light pulse having power intensity of 0.041–0.153 mW cm<sup>-2</sup> and pulse width of 1 s (interval of 10 s) was used. As a result, the device consumed an energy of 1.4 nJ per single event. Also, for habituation, an electrical pulse having pulse width of 10 ms (interval of 1 s) and pulse amplitude of 10 V was used. With pentacene, type 2 band alignment was formed, which played a crucial role in exciton separation

during light-assisted charge trapping and releasing processes. The photogenerated holes tend to migrate from the QDs to the pentacene layer, while the electrons remain in the conduction band. Also, the trapped electrons form an internal electric field, which accelerates the hole extraction to the semiconductor. Qian et al. reported planar structure optoelectronic synapse devices using a copper phthalocyanine (CuPc)/para-hexaphenylene (p-6 P) organic heterojunction.<sup>[47]</sup> Here, the channel had a dimension of 1000  $\mu$ m  $\times$  100  $\mu$ m. The photogenerated electrons are trapped at the p-6 P/dielectric interface, while the photogenerated holes in the CuPc channel increase the conductivity. For LTP, a light pulse having power of 0.1 and 0.4 mW and pulse width of 0.5 and 1 s was used. Also, for LTD, an electrical pulse having pulse amplitude of 10 V and pulse width of 0.1 s was used. Using the synaptic plasticity, the recognition of Modified National Institute of Standards and Technology (MNIST) images was performed with 70–80% of recognition rate using the artificial neural network simulation.

### 2.2.4. Organic-Based Devices

Yang et al. reported planar-diode-structure optoelectronic artificial synapse devices using diocylbenzothienobenzothiophene (C<sub>8</sub>-BTBT) material.<sup>[76]</sup> The channel had a dimension of 40  $\mu$ m  $\times$  20  $\mu$ m. In this work, two layers of C<sub>8</sub>-BTBT were optimized to have a high photosensitivity, low power consumption (13.6 pJ), and long-persisting photocurrent. The synaptic behavior was induced by the photogenerated excitons modulating the Schottky barrier height. Using the optimized device, neuromorphic functions such as STM and LTM were emulated. Also, a light pulse with power intensity of 16 mW cm<sup>-2</sup> and pulse width of 500 ms was used, with electrical bias of -2 V. Yin et al. reported planar structure optoelectronic synapse devices using a MAPbI<sub>3</sub>/silicon membrane structure.<sup>[77]</sup> The channel had a dimension of 500  $\mu$ m  $\times$  25  $\mu$ m. Light pulses having pulse width of 200 ms and power intensity of 1  $\mu$ W cm<sup>-2</sup> were used with an applied bias of 0.01 V. In the device, carriers generated by the light irradiation induced the photogating effect, which is also affected by the gate voltage. The device emulated remembering/forgetting of letters by modulating the levels of the photogating effect. Also, it was shown that the device consumed energy of 1 pJ per operation.

Hao et al. reported planar structure optoelectronic synapse devices using organic poly[2,5-(2-octyl)dodecyl]-3,6-diketopyrrolopyrrole-alt-5,5-(2,5-di(thien-2-yl)thieno [3,2-b]thiophene)] (DPPDTT) and perovskite (CsPbBr<sub>3</sub> QDs) hybrid.<sup>[78]</sup> The channel had a dimension of 30  $\mu$ m  $\times$  1000  $\mu$ m. In the device, photogenerated carriers are trapped in CsPbBr<sub>3</sub>, causing a built-in potential and consequently photogating effect and delayed recombination process. For optical writing, a light pulse with power of 0.06–1.20 mW cm<sup>-2</sup> (mainly 0.12–0.3 mW cm<sup>-2</sup>) and pulse width of 0.6–1 s was used, with a drain bias of -1 to -4 V. For erasing, an electrical pulse with width of 0.6 s (interval of 1.2 s) and amplitude of -3 V was used. In case of applying 0.2 V for drain and gate biases, the device showed a distinct optoelectronic synaptic behavior. Also, the device could operate at a low voltage of 0.005 V, having extremely low power consumption of 0.5 fJ per operation. Furthermore, by varying the pulse

number and the light intensity, the emulation of human visual memory was demonstrated.

Pradhan et al. reported planar structure optoelectronic synapse devices using a graphene/organic–inorganic halide PQD hybrid structure.<sup>[79]</sup> The device had a channel length of 15  $\mu\text{m}$ . When light is illuminated, photogenerated EHPs are dissociated by the built-in potential at the graphene/PQD interface, which then induce the photogating effect. As a result, the hole current is increased. For the operation, a light pulse having power intensity of 190–1.1  $\mu\text{W cm}^{-2}$  was used and the device had a power consumption of 36.75 pJ per spike. Chiang et al. reported planar structure photonic transistor–type nonvolatile memory devices.<sup>[80]</sup> Although this work is mainly concerned with memory devices, it can be also utilized in realizing optoelectronic neuromorphic devices. Here, the device was fabricated with two structures, 2,9-bis(2-phenylethyl)anthra[2,1,9-def:6,5,10-d'e'f']diisoquinoline/bis((2 E,6 E,10 E,14 E,18 E,22 E,26 E,30 E)-3,7,11,15,19,23,27,31,35-nonamethylhexatriaconta-2,6,10,14,18,22,26,30,34-nonaen-1-yl)3,3'-(1,3,8,10-tetraoxanthra[2,1,9-def:6,5,10-d'e'f']diisoquinoline-2,9(1 H,3 H,8 H,10 H)-diyl)dipropanoate (BPE-PDI/Sol-PDI) and dinaphtho-[2,3-b:2,3-f]thieno[3,2-b]thiophene/2,9-dicycldinaphtho-[2,3-b:2,3-f]thieno[3,2-b]thiophene (DNNT/C10-DNNT). Depending on the presence of Sol-PDI and C10-DNNT, which had a rod-coil structure, non-volatile memory characteristics were determined. It is suggested that the rod-coil type materials are suitable for the floating gate because of the charge trapping behavior. For programming, a light pulse having power intensity of 8–10  $\text{mW cm}^{-2}$  was used. Also, the device showed a high photocurrent up to  $10^5$  and low energy consumption.

Deng et al. proposed a three-terminal planar structure device using 2,8-difluoro-5,11-bis(triethylsilylethynyl) anthradithiophene (diF-TES-ADT) crystal arrays serving as a photoactive layer.<sup>[81]</sup> In dark condition, the device showed typical p-type transistor characteristics. Under light illumination ( $\lambda = 757 \text{ nm}$  and power intensity of  $10 \mu\text{W cm}^{-2}$ ), EHPs are generated in the active layer. After rapidly moving into oxygen-related levels, the electrons form  $\text{O}_2^-$  anions, whereas the holes are transferred from the active layer to the interface between the channel and insulator. Subsequently, the accumulated  $\text{O}_2^-$  anions push the holes into the diF-TES-ADT layer, causing a drastic increase of excitatory postsynaptic current (EPSC). After removing the light source, the injected holes gradually disappear due to the decreasing amount of  $\text{O}_2^-$  anions, which results in a decrease of the EPSC. Using the device, STP was emulated with a weak light pulse ( $7 \mu\text{W cm}^{-2}$ , 120 ms), and LTP with a more intense light pulse ( $30 \mu\text{W cm}^{-2}$ , 50 ms).

Dai et al. reported optoelectronic synaptic transistors fabricated with a polyacrylonitrile (PAN) insulator and a C8-BTBT organic channel layer.<sup>[82]</sup> Here, the PAN film was used to induce charge trapping effect at the PAN/C8-BTBT interface. Under UV light illumination ( $\lambda = 360 \text{ nm}$ , power intensity of  $0.90 \text{ mW cm}^{-2}$ ), a gradual positive threshold voltage shift was observed, which can be attributed to the compensation of trap sites with light-induced holes at the channel/insulator interface. When the light is turned off, the photogenerated holes are recaptured back to the trap sites, causing a negative threshold voltage shift and a positive displacement from the original current state. Using the device, neuromorphic behaviors such as STM and

LTM were mimicked by varying the number of light spikes (10, 30, 60, and 120), the pulse width (100, 200, 300, 400, and 500 ms), and the power intensity (0.16, 0.38, 0.61, and  $0.90 \text{ mW cm}^{-2}$ ).

### 2.3. Vertical Structure Devices

To increase the device density in neuromorphic circuits, down-scaling of neuromorphic devices is crucial. Typically, devices with nanometer scales are highly desired. In this perspective, the vertical structure optoelectronic neuromorphic devices are more suitable than the planar devices because they can have small device size due to the two-terminal structure. Therefore, lots of investigations are undergoing to develop vertical structure optoelectronic neuromorphic devices, even though there still exist several issues such as interference (crosstalk) between the devices and low photoelectric conversion efficiency.

An optoelectronic resistive random-access memory (ORRAM) is one of the attractive candidates for neuromorphic applications because of its high light-response characteristics. Using a vertically stacked Pd/MoO<sub>x</sub>/ITO device having a two-terminal structure, Zhou et al. demonstrated synaptic devices with both nonvolatile and volatile resistance switching behaviors modulated by an optical stimulus.<sup>[21]</sup> Here, it is claimed that the valence state change is responsible for the device operation under light stimulation. Under UV light ( $\lambda = 365 \text{ nm}$ ), the MoO<sub>x</sub> active layer absorbs the light and EHPs are generated. The photogenerated electrons are excited to the conduction band of the MoO<sub>x</sub> and the native H<sub>2</sub>O molecules trigger the reaction with photogenerated holes, generating protons ( $\text{H}^+$ ). To verify the effectiveness of mimicking the human visual systems, image training and image recognition were conducted. The recognition rate and the efficiency were enhanced with the use of the ORRAMs.

Gao et al. proposed a simple vertically stacked ITO/Nb-doped SrTiO<sub>3</sub> (Nb:SrTiO<sub>3</sub>) heterojunction structure for an artificial optoelectronic synapse device (Figure 2a).<sup>[22]</sup> Here, the heterojunction structure is one of the key factors to emulate various synaptic functions such as PPF, STM/LTM, and learning behavior. Figure 2b shows the operation mechanism of the ITO/Nb:SrTiO<sub>3</sub> heterojunction artificial synapse device. Without light, the device is at a high-resistance state due to the large Schottky barrier height/width at the ITO/Nb:SrTiO<sub>3</sub> interface. These eventually prohibit the tunneling leakage current flowing in the device. By applying visible light illumination with an intensity of  $30 \text{ mW cm}^{-2}$  accompanied by an electrical bias, the level of resistance state was lowered due to the narrowing of the Schottky barrier height and the width. To validate the utilization of the device in neuromorphic applications, STM and LTM behaviors were mimicked by varying the pulse number or the frequency of blue light ( $\lambda = 400 \text{ nm}$ ) having pulse width of 0.5 s (Figure 2c). It was shown that the synaptic weight was gradually changed from STM to LTM with an increase of pulse number from 1 to 100, or the frequency from 0.05 to 1 Hz.

He et al. also reported memristor devices using a MoS<sub>2</sub> monolayer on a p-Si substrate (W/MoS<sub>2</sub>/SiO<sub>2</sub>/p-Si) for high-density large-scale neuromorphic chips (Figure 2d).<sup>[83]</sup> When the device

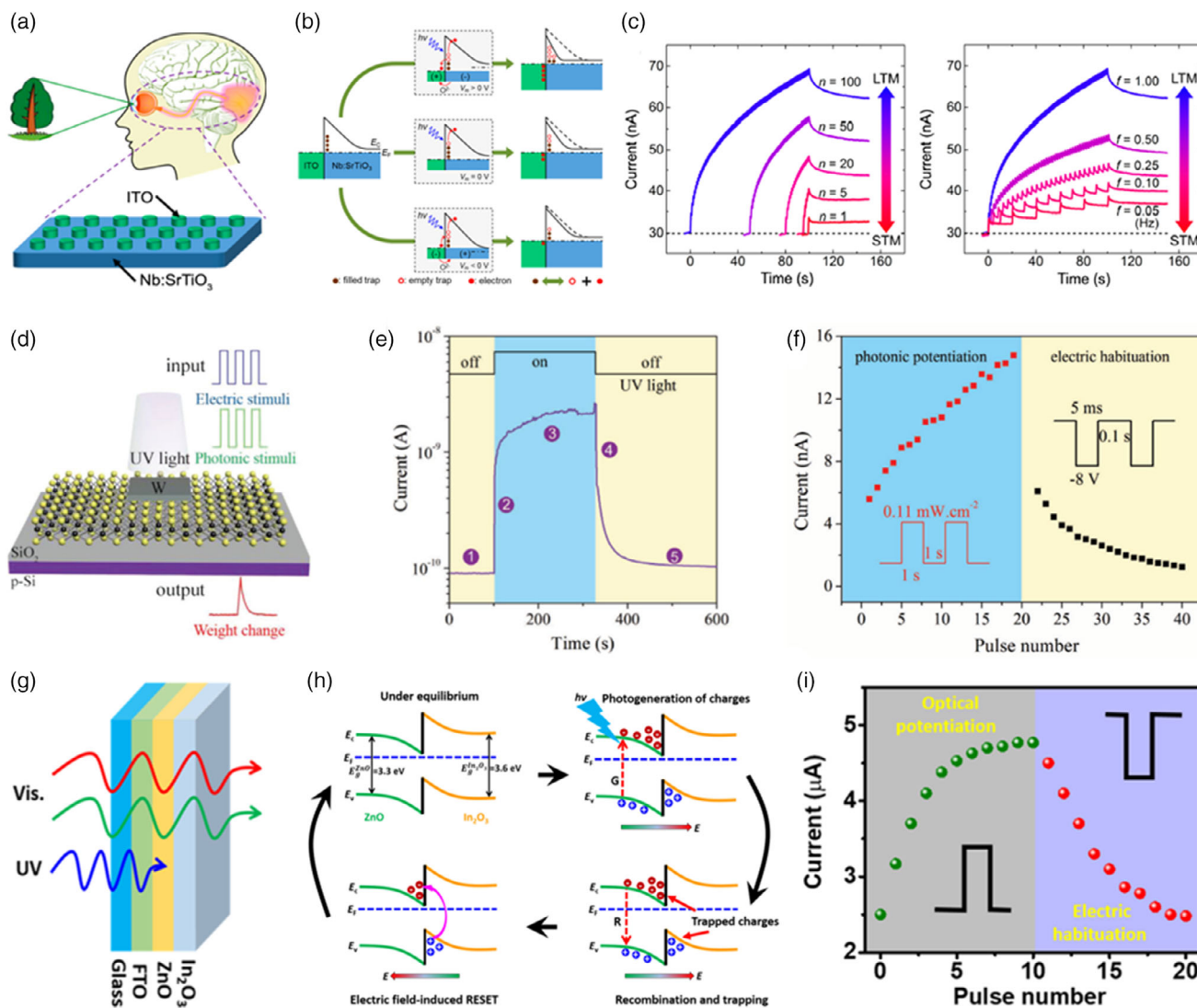


**Figure 2.** a) The concept and schematic device structure of a vertical structure ITO/Nb:SrTiO<sub>3</sub>-based optoelectronic synapse device emulating the human visual system. b) The operation mechanism of the ITO/Nb:SrTiO<sub>3</sub> synapse device. The variation of Schottky barrier profile under different stimulation conditions. c) The emulation of STM and LTM behaviors by varying the number and frequency of the light stimuli. (a–c) Reproduced with permission.<sup>[22]</sup> Copyright 2019, American Chemical Society. d) The schematic device structure of a MoS<sub>2</sub>-based memristive synapse. e) Typical PPC behavior induced by a light stimulus. f) A demonstration of optically modulated potentiation and electrically modulated habituation. (d–f) Reproduced with permission.<sup>[83]</sup> Copyright 2018, Wiley-VCH. g) The device structure of a vertical structure FTO/ZnO/In<sub>2</sub>O<sub>3</sub>-based optoelectronic synapse device. h) The operation mechanism of the FTO/ZnO/In<sub>2</sub>O<sub>3</sub> synapse device. i) A demonstration of optically modulated potentiation and electrically modulated habituation. (g–i) Reproduced with permission.<sup>[84]</sup> Copyright 2018, American Chemical Society.

was irradiated with UV light ( $\lambda = 310$  nm) having power intensity of  $0.11 \text{ mW cm}^{-2}$ , EHPs were generated and increased the electrical conductance (Figure 2e). When the light was off, the current dropped relatively slowly, exhibiting PPC behavior. As shown in Figure 2f, the potentiation and habituation processes were conducted by applying light (intensity of  $0.11 \text{ mW cm}^{-2}$  and pulse width of 1 s) and electrical bias (amplitude of  $-8$  V and width of 5 ms). In addition, vertically stacked ZnO/In<sub>2</sub>O<sub>3</sub>-based synaptic devices were reported by Kumar et al.<sup>[84]</sup> As shown in Figure 2g, the device was composed of fluorine-doped tin oxide (FTO)/ZnO/In<sub>2</sub>O<sub>3</sub> layers, in which the type-II band alignment is formed between the ZnO and In<sub>2</sub>O<sub>3</sub> layers. This

allowed the trapping of photogenerated charge carriers under light illumination and the PPC effect. Figure 2h shows the operation mechanism of the device under various operation conditions. At an equilibrium state, due to the higher electron affinity of ZnO compared to In<sub>2</sub>O<sub>3</sub>, band bending occurs at the interface. Subsequently, with UV illumination, EHPs are generated and the holes and electrons move toward the In<sub>2</sub>O<sub>3</sub> and ZnO, respectively. When the light is off, the trapped charges remain near the interface, causing a reduction of the effective barrier height and the PPC behavior. With a negative bias, these trapped charges are recombined, returning to the original state. Using these characteristics, light-triggered (power intensity of

$0.4 \text{ mW cm}^{-2}$ ) potentiation and electrical bias-triggered (amplitude of  $-1 \text{ V}$  and duration of  $20 \text{ ms}$ ) habituation were demonstrated, as shown in Figure 2i. Furthermore, the device exhibited energy consumption of  $0.2 \text{ nJ}$  when the pulse duration was  $5 \text{ ms}$ .

Tan et al. also reported an optoelectronic device having a vertically stacked ITO/CeO<sub>2-x</sub>/AlO<sub>y</sub>/Al structure. Here, the conductivity was modulated by using visible light (power intensity of  $6 \text{ pW } \mu\text{m}^{-2}$ ) and electrical bias.<sup>[46]</sup> Due to the detrapping/retrapping of electrons in the interfacial CeO<sub>2-x</sub> layer positioned next to the AlO<sub>y</sub> layer, the band bending of the CeO<sub>2-x</sub>/AlO<sub>y</sub>/Al region could be controlled. Using the ITO/CeO<sub>2-x</sub>/AlO<sub>y</sub>/Al device with light and electrical stimuli, basic Boolean binary logics of reconfigurable AND, OR, and NOT operations were demonstrated.<sup>[45]</sup> Oxide-based perovskite materials can also be promising material candidates for optoelectronic neuromorphic devices because of their decent light-response characteristics.<sup>[85]</sup> Bera et al. reported a vertical structure light-switchable memory device using Wurtzite ZnO on perovskite SrTiO<sub>3</sub>.<sup>[86]</sup> When the device was applied with UV light ( $\lambda = 365 \text{ nm}$  and power intensity of  $2.5 \text{ mW cm}^{-2}$ ), photogenerated, electrons were trapped, leading to a high conductance state. Also, the PPC behavior was observed which originated from the slow drifting of the ionized oxygen vacancies. Multilevel data storage was demonstrated utilizing the multiple resistance states.

Yang et al. reported vertical structure synapse devices using a BiFeO<sub>3</sub>/SrRuO<sub>3</sub> (BFO/SRO) heterostructure. Here, opposite to conventional optoelectronic devices, the optical excitation induced a decrease in electrical conductivity.<sup>[72]</sup> Because the as-grown BFO active layer on the SRO bottom electrode was spontaneously downward polarized, a negative polarization charge was created near the top BFO surface. This would cause positively charged oxygen vacancies to move toward the top BFO surface during the high-temperature deposition process. At the initial state, these positively charged oxygen vacancies were compensated for by the electrons in the space-charge region. However, under light illumination (power intensity of  $10 \text{ mW cm}^{-2}$ ), the electrons needed to neutralize the positively charged oxygen vacancies were driven to the ITO layer, resulting in widening and increasing of the energy barrier. As a result, the resistance was increased. On the other hand, when negative electrical pulses were applied, the electrons migrated to the ITO layer were injected back to the original state, decreasing the resistance.

Moreover, Wang et al. reported optoelectronic synapse devices using an eutectic gallium indium/poly-L-histidine/Au nanorod stacked structure.<sup>[87]</sup> Here, it was shown that the nanorod stacked device could be optically programmed with light having power intensity of  $0.03 \text{ W cm}^{-2}$  ( $\lambda = 500\text{--}750 \text{ nm}$ ), which induced plasmonic excitation in the device. Hu et al. reported a vertically structured two-terminal synaptic device using a ZnO<sub>1-x</sub>/AlO<sub>y</sub> heterojunction.<sup>[88]</sup> Here, the defects in the AlO<sub>y</sub> layer had the role of charge trapping, enabling the mimicking of synaptic plasticity. Particularly, light pulses were used for potentiation and electrical pulses for depression. With the light illumination, EHPs were generated, resulting in an increase of conductance. The photogenerated holes migrated to the interface and were trapped in the AlO<sub>y</sub> layer. Subsequently, the removal of the light caused the holes to be detrapped back to their original states, resulting

in the PPC behavior. For the operation of the device, a light pulse having power intensity of  $0.005\text{--}0.0742 \text{ mW cm}^{-2}$  and pulse width of  $1 \text{ s}$  (interval of with  $1 \text{ s}$ ) was used. Also, an electrical pulse with amplitude of  $-4 \text{ V}$  and width of  $10 \text{ ms}$  was used (interval of  $100 \mu\text{s}$ ).

Ren et al. reported a  $5 \times 5$  vertical structure optoelectronic memristor array using ZnO-phosphorene nanoparticles (ZP NPs) sandwiched in PMMA.<sup>[89]</sup> ZnO is well known as an anion-based switching material forming oxygen vacancy filaments. Here, the phosphorene acted as effective trapping sites. Under light illumination, photogenerated EHPs are separated at the heterojunction inside the ZP NPs, and then the photogenerated holes are trapped in the NPs acting as a local gate modulating the conductivity. Here, a light pulse having various wavelengths ( $\lambda = 380, 532, \text{ and } 633 \text{ nm}$ ), pulse interval of  $0.01\text{--}1 \text{ s}$ , and power intensity of  $0.05 \text{ mW cm}^{-2}$  was used for the operation. Also, electrical biases of  $1$  and  $5 \text{ V}$  were used for reading and spiking events, respectively. Jaafar and Kemp reported optoelectronic nonvolatile memory devices in both planar (interlocked electrodes) and vertical (island electrodes) structures using GOs.<sup>[90]</sup> The device was fabricated having a gap between the electrodes ( $50 \mu\text{m}$ ) for planar structure and a circular electrode with diameter of  $400 \mu\text{m}$  for vertical structure. The conduction mechanisms and the operation of the devices were different for the planar- and vertical-structured devices that originated from the forming process. For the planar device, an electrical bias with amplitude of  $-2$  to  $2 \text{ V}$  was applied. Also, a light pulse with various wavelengths ( $\lambda = 625, 525, \text{ and } 465 \text{ nm}$ ), light intensity of  $44 \text{ mW cm}^{-2}$ , and pulse width of  $60 \text{ s}$  (interval of  $60 \text{ s}$ ) was applied to the device while biased with  $0.1 \text{ V}$ . For the vertical device, an electrical bias of  $-1$  to  $1 \text{ V}$  was applied with the light stimuli used identical to those used for the planar-structured device. Because the vertical structure had a shorter pathway, it exhibited a higher on/off ratio. In addition, Ham et al. reported vertically stacked optoelectronic synaptic devices inspired by dopamine-facilitated synaptic activity, using an organolead halide perovskite material, CH<sub>3</sub>NH<sub>3</sub>PbI<sub>3</sub>.<sup>[48]</sup> In this work, the mechanism under light stimuli was explained by the identical direction of the photogenerated electric field with the external electric field. When light with an intensity of  $10 \text{ mW cm}^{-2}$  was irradiated on the device, the electric field was increased due to the photogenerated EHPs, increasing the total electric field and lowering the formation energy. Using the CH<sub>3</sub>NH<sub>3</sub>PbI<sub>3</sub>-based synaptic device, an accuracy of  $82.7\%$  was achieved in MNIST pattern recognition after  $2000$  learning phases.

As previously mentioned, various materials and vertical structures have been investigated to realize optoelectronic neuromorphic devices. It is considered that by adopting the two-terminal crossbar structure for a device similar to the electrical memristor or synapse devices, advantages such as high-density integration and low-voltage operation could be attained. Although nanoscale optoelectronic synaptic devices have not been fully demonstrated yet, supposedly due to the difficulties in obtaining nanoscale device structures and high power conversion efficiency, further investigations are still worth conducting to demonstrate the applicability of optoelectronic neuromorphic devices in high-density integrated circuits.

### 3. All-Optical Neuromorphic Devices

#### 3.1. Phase Change Material (PCM)-Based Memory and Neuromorphic Devices

As described, all-optical integrated circuits can have advantages such as high processing speed, parallel processing, high energy efficiency, and low crosstalk. However, all optical operating systems have not been much investigated yet due to the complexity of the device structure and their operations. Recently, PCM-based all-optical memory devices were demonstrated, which could be further utilized in neuromorphic computing. Particularly, PCM-based devices are one of the most promising candidates for all-optical photonic chips due to their memorization capability. Here, the optical signal that has a considerable amount of energy can be converted to thermal energy, which then transforms the crystalline phase of the PCMs. The changed phase state exhibits different light transmission properties apart from its original state, which can be used for nonvolatile memorization function.

Ríos et al. reported a nonvolatile multilevel memory operated only by optical signals.<sup>[91]</sup> In this report,  $\text{Ge}_2\text{Sb}_2\text{Te}_5$  (GST) was utilized as the light absorbing layer, which transforms from crystalline to amorphous phase by light. Particularly, when optical pulses with sufficient energy are irradiated into the GST cell, heat is generated, which subsequently melts the GST locally. Then, after quenching, the region becomes an amorphous state (write process). Afterward, when the GST cell absorbs sufficient energy for crystallization by a higher power light pulse, it transforms into the crystalline state as an erase process. Because the crystalline GST phase has higher reflectivity, this attenuates the reading pulse compared to the amorphous phase GST. The reading pulses have insufficient energy for phase transformation and interact with the GST, which results in nonvolatile optical

transmission data of “0” and “1,” as digital signals. Because all the operations were conducted using the light, the device only consumed  $\approx 500$  ps of time and  $\approx 480$  fJ of energy for the operation. Furthermore, waveguides were used to deliver the optical signals into the GST cell for write and erase processes.

Later on, Cheng et al. demonstrated a PCM-based all-optical memory device to realize a chip-level photonic synapse device.<sup>[20]</sup> Here, chalcogenide GST was used for the PCM cells, which was capped by an ITO layer. The PCM cell had a dimension of  $1 \times 3 \mu\text{m}^2$ , and the whole device was fabricated with a size of few hundreds of  $\mu\text{m}^2$ . Here, to improve the controllability of the electric field of the optical pulses, a taper-structured waveguide with multiple discrete PCM cells was used, as shown in **Figure 3a–c**. For the optical signals, pulses having width of 50 ns and power of 1 W were used, resulting in energy consumption of 243–320 pJ per operation. As shown in **Figure 3d**, the transmission change was distinguishable for up to 40 switching cycles, showing the long-term durability of the switching characteristics. With the device, the STDP plasticity was emulated by adding an interferometer and a phase modulator (PM). The time difference of the presynaptic signal and the postsynaptic signal affected the synapse weight change (**Figure 3e**). The input (presynaptic signal) and output (postsynaptic signal) signals could be divided through a circuit, giving a feedback on the synapses (**Figure 3f**). Depending on the spiking time difference between the input and output signals, the number of pulses over a certain threshold switching power that were sent to the synapse was changed (**Figure 3g–k**).

More recently, Feldmann et al. demonstrated all-optical multisynapse networks with self-learning capabilities.<sup>[92]</sup> Here, four presynapses consisting of GST and waveguides were connected to a neuron. The device was fabricated with a size of  $1500 \mu\text{m} \times 300 \mu\text{m}$ , and a waveguide having a width of  $1.2 \mu\text{m}$  was implemented. Each presynapse had a ring resonant

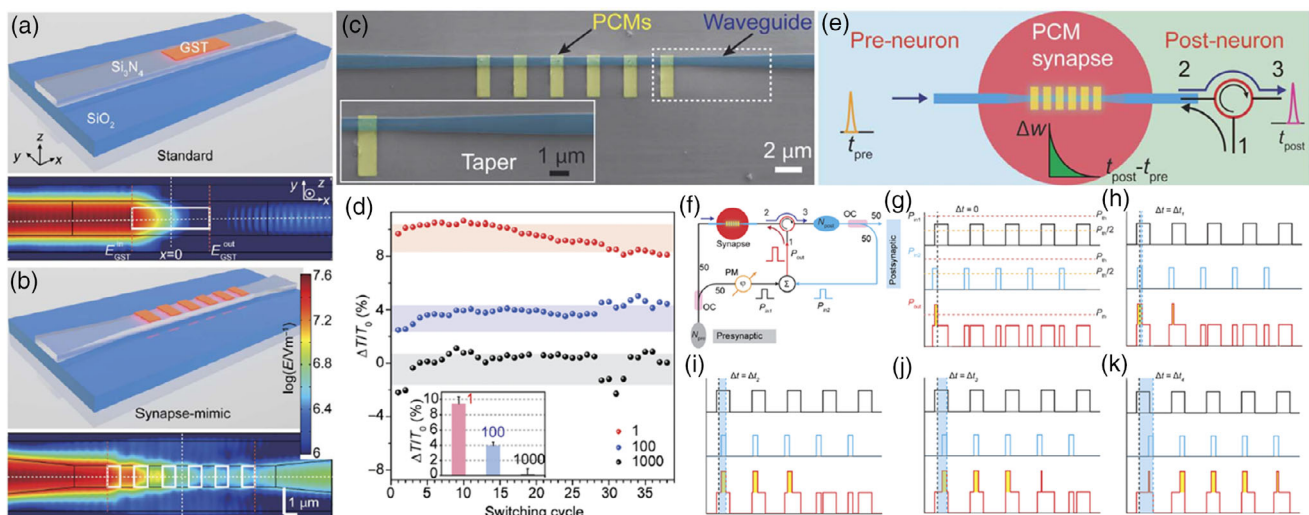


**Figure 3.** Schematic structures of PCM-based all-optical synapse a) with a single GST island and b) with six discrete GST islands. c) A scanning electron microscope image of the tapered waveguides and the island-structured PCMs. d) The variations of transmittance (weighting) in multiple switching cycles. e) A conceptual schematic of the integrated photonic synapse with pre- and postneurons. f) Operation schematic of the all-optical method for emulating the STDP behavior. g–k) The emulation of STDP behavior using all-optical synapse devices. (a–k) Reproduced with permission.<sup>[20]</sup> Copyright 2017, American Association for the Advancement of Science.

component to have a wavelength selectivity of the input signal and a light signal having pulse width of 200 ns was used. The input signal then could update the transmittance of the PCM, which corresponded to the synaptic weight. The weight updating relied on the typical PCM memory storage mechanism. For example, if the PCM cell was in amorphous phase, the light transmission was higher, which was regarded as a strong synaptic connection. Depending on the integrated signals combined from the presynapses, the crystalline phase of the neuronal PCM could be changed, determining whether to generate an output signal. Particularly, the output signal was generated only when merged input signals had a sufficient energy over a threshold value, similar to the integrate-and-fire behavior observed in the biological neural network. Furthermore, a pattern classification was successfully demonstrated using the all-photon network.

### 3.2. Nanocavity-Based Photonic Memories

By adopting a nanocavity structure, confinement of photons is possible which can be utilized to realize the memory function. Nanocavities have been widely researched in nanophotonics, such as lasers, quantum communication, quantum emitters, and photonic chips.<sup>[93–99]</sup> Among these applications, an optical switch and all-optical memory devices utilizing nanocavities have been reported previously.<sup>[100–102]</sup> Although currently these devices are not intended for use in neuromorphic computing, it is expected that their memorization functions utilizing light can be, in the near future, used for neuromorphic applications. Therefore, nanocavity devices are promising candidates in future optoelectronic neuromorphic devices. In nanocavity devices, the periodic difference of the dielectric constant can form a photonic bandgap, which prevents the propagation of photons at a certain range of frequencies. The photonic bandgap can hold photons with a resonance by the quantum confinement effect.<sup>[103]</sup> Generally, the material's ability of holding the photons (keeping resonance) is represented by the  $Q$ -factor.<sup>[104]</sup> For instance, when the  $Q$ -factor is high, the energy loss at the edge of the periodic structure is low. Silicon has been used for nanocavity devices because of the vast nanopatterning technology, but recently, more diverse materials are being studied. Also, the propagating light can be manipulated by placing defects at the middle of the cavity array.<sup>[105]</sup>

Nozaki et al. reported nanocavity structure-based all-optical memory devices.<sup>[106]</sup> The nanocavities were fabricated within an InP substrate, and InGaAsP (for buried heterostructure) was placed at the middle of the InP for increasing the  $Q$ -factor and heat escaping purpose. A single structure was fabricated with a size of less than  $10 \mu\text{m}^2$  and the whole device was integrated in a size of  $10 \text{mm}^2$ . When a high power pump light was applied, photogenerated carriers distorted the wavelength spectra, where the degree of distortion increased with the light power.<sup>[107]</sup> Here, a light signal having a power intensity of 30 nW was used and the 1 Mbit device operation consumed 100 mW per switching. Kuramochi et al. reported nanocavity structure wavelength-addressable all optical memory devices.<sup>[108]</sup> Similar to the study mentioned earlier, the nanocavities were fabricated within InP, where InGaAsP was buried in the middle of the cavities. In this work, bistable cavities that had nonidentical resonance

wavelengths were parallelly placed, sharing a common waveguide. When different wavelengths of input signals passed through the waveguide, they selectively distorted the wavelength spectra. With the device, 28 bit RAM operation was emulated, consuming  $137 \mu\text{W}$  of power. Here, a light pulse having pulse width of 100 ps, energy of 100–270 and 30–70 fJ was used for writing and reading, respectively, with an electrical bias having power of 1.6–13  $\mu\text{W}$ .

## 4. Applications of Optoelectronic Neuromorphic Devices

### 4.1. Artificial Visual Systems

Because the optoelectronic synapse devices use light signals as the input stimuli, mimicking optic nerves and visual systems has been demonstrated due to their resemblance. Kwon et al. recently reported an environment-adjustable photonic synapse circuit.<sup>[49]</sup> The circuit consists of an ionotronic synaptic transistor and a photovoltaic divider consisting of a load transistor and a photosensor (Figure 4a,b). The ionotronic synaptic transistor is constructed with an amorphous IGZO channel and a Na-incorporated  $\text{Al}_2\text{O}_3$  gate dielectric layer. In this transistor, synaptic behavior can be emulated using the gate bias spikes ( $V_{\text{spike}}$ ), which cause the Na ions to migrate in the layer. As a load transistor, amorphous IGZO thin-film transistors (TFTs) with low light-responsivity to visible light was used. Also, for the photosensor, a CdSe layer with high light responsivity was used. For the light input, light with power intensity of  $7.5\text{--}43.5 \text{mW cm}^{-2}$  and pulse width of 0.5 s was used. Also, electrical biases of 1 or 3 V for drain voltage, 0.2–0.26 V for load voltage, and 2 V for spiking were used. Figure 4c shows a  $3 \times 3$  array of the optoelectronic neuromorphic circuits. To emulate the photopic and scotopic adaptations (Figure 4d,e), the load gate voltage can be adjusted to change the visual threshold depending on the light intensity. In this way, environment (light intensity)-adaptable visible systems can be realized (Figure 4f,g).

The human eyes can recognize the patterns of visual information as well as colors. Seo et al. reported an artificial optoelectronic synapse device perceiving a mixed colored pattern by utilizing a h-BN/WSe<sub>2</sub> heterostructure (Figure 4h).<sup>[26]</sup> Red ( $\lambda = 655 \text{nm}$ ), green ( $\lambda = 532 \text{nm}$ ), and blue ( $\lambda = 405 \text{nm}$ ) light sources were used with identical power intensity ( $6 \text{mW cm}^{-2}$ ). The input pulse was  $\pm 0.3\text{--}1 \text{V}$  with pulse width of 10 ms. Here, shorter wavelength incident light can trap more carriers in the weight control layer (h-BN), which then increases the conductivity of the channel. When the device is stimulated by high-amplitude pulses, the charge carriers are trapped in the “slow traps,” which have a slow detrapping time compared to the “fast traps” (Figure 4i). The applied bias was 0.1 or 1 V depending on the intended trapping mechanism. As a result, the device consumed an energy of 66 to 532 fJ per operation. As each wavelength of light shows a different amount of PSC change, the synaptic device can classify each of the colors, as shown in Figure 4j,k. In addition, the device can be used in the pattern recognition of a color-mixed MNIST dataset, providing a similar level of accuracy compared to noncolored pattern recognition.

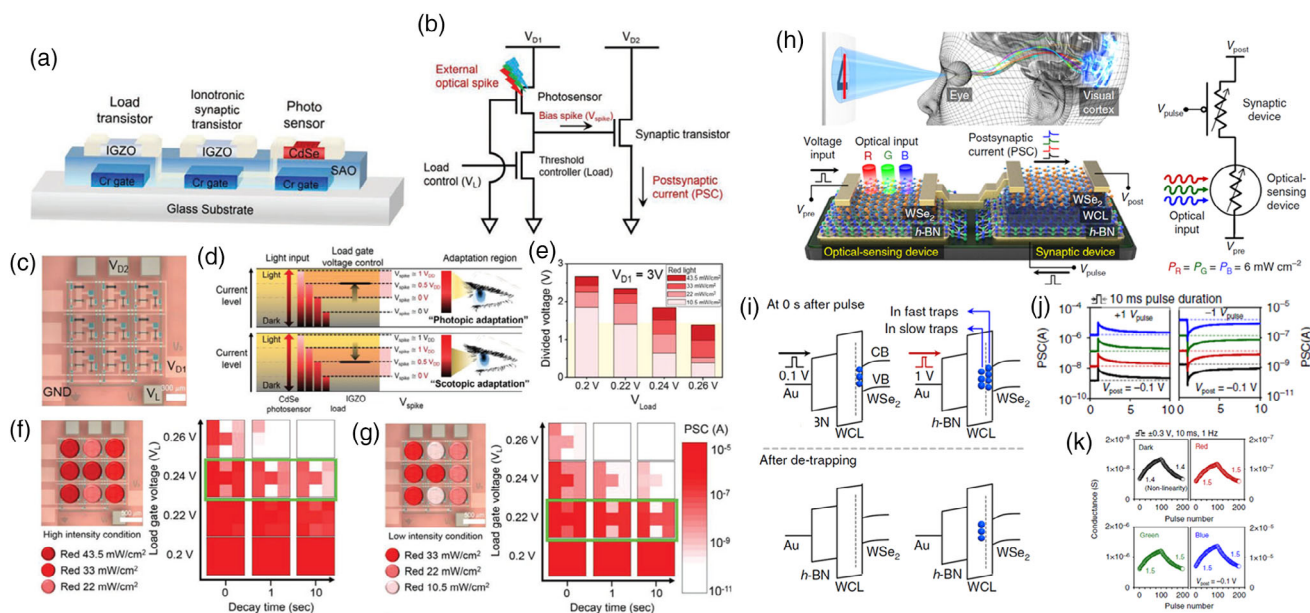


**Figure 4.** a) The configuration and b) circuit diagram of an artificial visual perception system. c) An optical image of the  $3 \times 3$  optoelectronic neuro-morphic circuit array. d) Schematics of the mechanism for photopic and scotopic adaptations. e) Variation of the divided voltage under various light illumination and loading voltage conditions. Optical images and encoded images obtained from the array under f) high-intensity light condition and g) low-intensity light condition. (a–g) Reproduced with permission.<sup>[49]</sup> Copyright 2019, Wiley-VCH. h) Schematic of an optical nerve system and the structure of the circuit comprising h-BN/WSe-based synaptic device and photodetector. i) Energy band diagrams showing the trapping/detrapping mechanisms. j) Excitatory and inhibitory PSC variation and k) the LTP/LTD characteristics under different light illumination. (h–k) Reproduced with permission.<sup>[26]</sup> Copyright 2018, Springer Nature.

## 4.2. Artificial Motor Nerve Systems

Emulation of artificial biological motor nerves also has been demonstrated. Recently, Tan et al. reported artificial afferent nerve systems by combining a pressure sensor and an optoelectronic synaptic device. The pressure sensor was fabricated with

$\text{Ti}_3\text{C}_2\text{T}_x$  MXene and could generate output signals depending on the pressure intensity. Particularly, when the pressure sensor is stimulated, a voltage signal is generated, which is in turn changed into an optical pulse by an analog-to-digital converter (ADC) and a light-emitting diode (LED) (Figure 5a,b).<sup>[109]</sup> Converted signals are then transmitted through an optical fiber

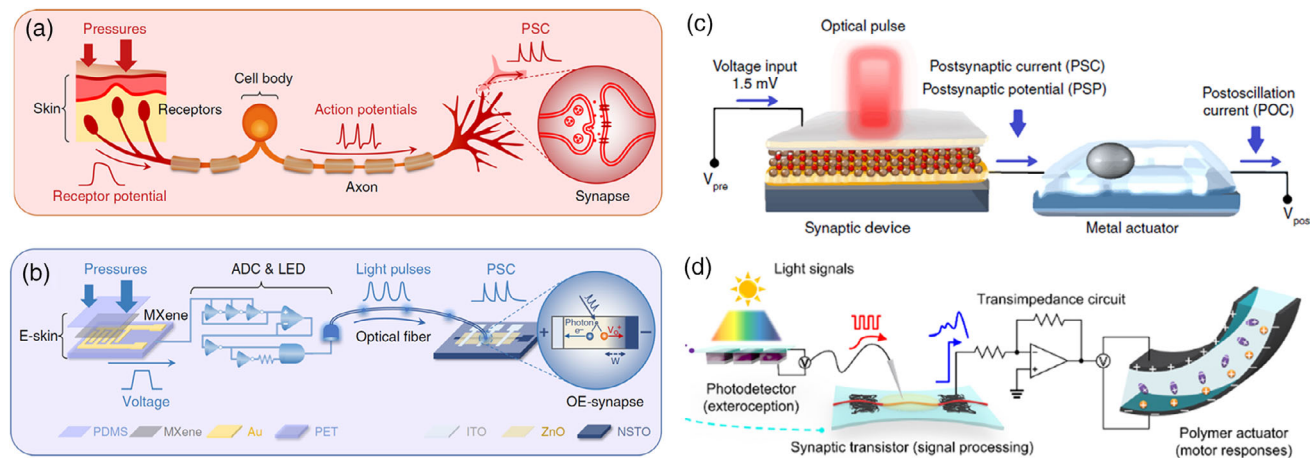


**Figure 5.** a) Schematic of a biological sensory system comprising receptors, cell body, neuron, and synapses. b) A schematic structure of the artificial sensory system for mimicking the biological sensory system. Here, the flexible pressure sensor acts as skin, generating voltage signals when stimulated. Then, light pulses are generated from the ADC and LED circuit. (a,b) Reproduced with permission.<sup>[109]</sup> Copyright 2020, Springer Nature. c) A schematic structure of the sensorimotor system consisting of a synaptic device and a metal actuator. Reproduced with permission.<sup>[50]</sup> Copyright 2019, Springer Nature. d) The structure and operation scheme of an optoelectronic sensorimotor synapse. Reproduced with permission.<sup>[110]</sup> Copyright 2018, American Association for the Advancement of Science.

to the ITO/ZnO/Nb-doped SrTiO<sub>3</sub> (NSTO) optoelectronic synapse device. Due to the ZnO/NSTO interface, the device could exhibit PPC behavior. As a possible application, the recognition of handwritten words was demonstrated. Here, a light source having wavelength of 375 nm, power intensity of  $0.65 \pm 0.06 \text{ mW mm}^{-2}$ , and pulse width of 1 ms was used. Also, the synaptic photomemristor was fabricated with an area of  $100 \mu\text{m}^2$ .

Akbari and Zhuiykov reported artificial neurobotics consisting of an optical synaptic device and a metal actuator device.<sup>[50]</sup> The synaptic device was fabricated with an indium-doped TiO<sub>2</sub> photomemristor that exhibits complementary resistive switching behavior with the light signal. Particularly, pulsed laser light ( $\lambda = 530 \text{ nm}$ ) was applied with a duration of 250 ms per pulse and power intensity of  $7\text{--}100 \mu\text{W cm}^{-2}$ . Also, a constant bias (1.5 mV) was applied to the device. As a result, the synaptic device consumed an energy of 2.41 pJ per event. The photocurrent generated from the photomemristor is transferred to the metal actuator, inducing a postoscillation current (Figure 5c). This work demonstrated that the synaptic device can convert a light stimulus into electrical and mechanical oscillation signals, which could be potentially used in optically driven neurobotics. In addition, Lee et al. reported optically operated artificial muscles utilizing a stretchable organic nanowire synaptic transistor, photodetector, and polymer actuator (Figure 5d).<sup>[110]</sup> Depending on

the input signal spikes, the excitatory postsynaptic current amplitude from the synaptic transistor could be modulated and consequently the displacement of the polymer actuator.

### 4.3. Pavlov's Dog Experiment

The most well-known animal behaviorism experiment, the Pavlov's dog experiment has been actively investigated using neuromorphic devices. Recently, Cho et al. reported emulation of Pavlov's dog behavior using CdS/ZTO heterostructure-based optoelectronic synaptic devices (Figure 6a).<sup>[51]</sup> Figure 6b,c shows the emulation of "feeding food" and "bell ringing" in Pavlov's dog experiment, respectively, using different light stimuli. Each of the stimuli can induce a PSC variation corresponding to the type of the stimuli. After conditioning with feeding and bell ringing stimuli, which were applied to the device simultaneously, the bell ringing stimulus could induce a sufficient PSC change over the threshold value, as shown in Figure 6d. After extinction, the unconditioned state is restored and the bell ringing could not generate a sufficient PSC over the threshold value (Figure 6f). Similarly, Kumar et al. reported the Pavlov's dog experiment by using ZnO/Ag nanowire-based flexible optoelectronic synaptic devices.<sup>[111]</sup> In this experiment, a light pulse having power intensity of  $4 \text{ mW cm}^{-2}$  and pulse width of 1 s was used. The device consumed an energy of  $\approx 4 \mu\text{J}$  per

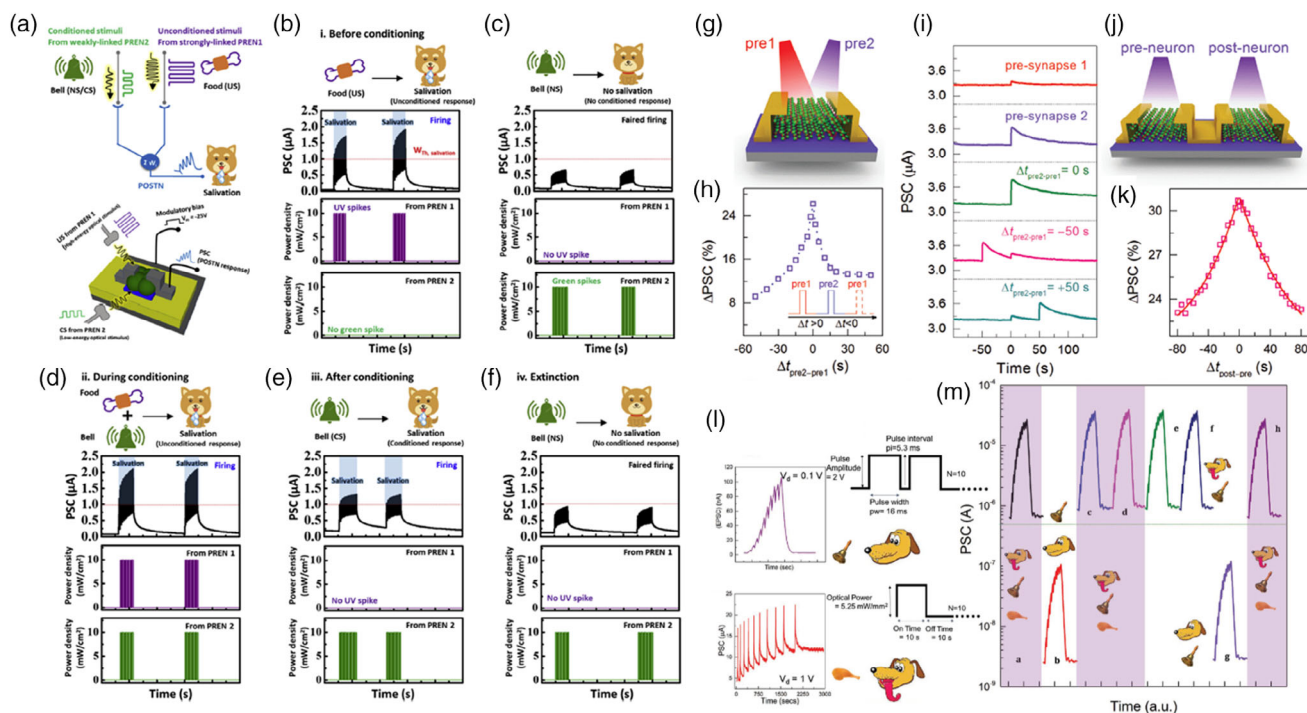


**Figure 6.** a) Schematics showing the concept of Pavlov's dog experiment using the neuromorphic devices and the device structure of a CdS/ZTO-based optoelectronic synaptic device. Here, the optical and electrical stimuli correspond to the conditioned (bell ringing) and unconditioned (food feeding) stimuli, respectively. b–f) The emulation of Pavlov's dog experiment using various combinations of light stimuli. (a–f) Reproduced with permission.<sup>[51]</sup> Copyright 2019, Elsevier B.V. g) The structure of a BP-based synapse device and a multineural system using two different light sources. h) The PSC variation depending on the time difference between two light inputs. i) The PSC variation under a single and a pair of light stimuli with a time difference. j) Schematic of the device layout to emulate the STDP behavior. k) The PSC variation depending on the time difference of pre-/postsynaptic pulses. (g–k) Reproduced with permission.<sup>[112]</sup> Copyright 2019, Wiley-VCH. l) The PSC variations under voltage and optical pulses that correspond to bell ringing and feeding food, respectively. m) The demonstration of Pavlov's dog experiment. (l,m) Reproduced with permission.<sup>[113]</sup> Copyright 2018, Wiley-VCH.

single spike. Because the device was fabricated with a relatively large dimension ( $\approx 0.6 \text{ cm}^2$ ), a considerably high energy was required for the operation, and it is expected that downscaling of the device size could reduce the energy consumption. Also, Ahmed et al. reported the Pavlov's dog experiment using BP and native phosphorus oxide ( $\text{PO}_x$ )-based optoelectronic synaptic devices.<sup>[112]</sup> The device was fabricated with a dimension of  $9.2 \pm 1.1 \text{ }\mu\text{m}^2$ . Here, depending on the spiking time difference, a PSC change could be induced, emulating the STDP characteristics (Figure 6g–i). Also, by varying the spiking time, linear variation of PSC was observed, as shown in Figure 6j,k. Here, a light pulse having pulse width of 100 ms and power intensity of  $3\text{--}10 \text{ mW cm}^{-2}$  was applied, at an applied bias of 10 mW. The device consumed energy of 3.5 pJ and  $9.24 \times 10^2 \text{ pJ}$  for optical and electrical synaptic activity, respectively. The combination of optical and electrical pulses could also be used to conduct the Pavlov's dog experiment. John et al. reported optoelectronic artificial synaptic devices using an ion-gel-gated  $\text{MoS}_2$  channel.<sup>[113]</sup> In the Pavlov's dog experiment, the electrical pulse is used as the bell ringing stimulation and the optical pulse as the feeding (Figure 6l). An electrical pulse with pulse width of 16 ms and amplitude of 2 V was applied at the back gate. For the light pulse, pulse width of 10 s and power intensity of  $5.25 \text{ mW mm}^{-2}$  was used with 1 V of drain bias. The device showed relatively high power consumption of  $52.5 \text{ mJ cm}^{-2}$  per event compared to the electrically operating mode (3 nJ per event). After repetitive training with these stimuli, only the bell ringing could evoke salivation behavior, as shown in Figure 6m.

## 5. Conclusion

In this review, we have discussed recently reported optoelectronic and all-optical neuromorphic devices which could be potentially used in artificial neuromorphic systems. In particular, we reviewed their device structures, constituting materials, operation mechanisms as well as the possible applications. To achieve photonics-based neuromorphic systems, aforementioned devices have been developed, partially realizing the emulation of important synaptic and neural behaviors of the human brain. Also, many interesting and prospective demonstrations of photonics-based neuromorphic devices have been achieved, such as artificial vision systems, motor systems, and emulation of the Pavlov's dog experiment. Beyond these outstanding and significant demonstrations, there still remain significant challenges to fully realize photonics-based neuromorphic systems. Particularly, a high-density chip-level array should be developed to demonstrate the feasibility of photonic neuromorphic systems. Also, the integration of light sources and enhancing the energy efficiency in photoelectric conversion should be further developed. Nevertheless, the review reported here implies that the photonics-based neuromorphic systems hold great promise in achieving highly energy-efficient and high-speed computing systems mimicking the functionality of the human brain.

## Acknowledgements

S.S. and J.K. contributed equally to this work. This work was supported by the National Research Foundation of Korea (NRF) grant funded by the

Korea Government (Ministry of Science and ICT) (No. NRF-2017R1E1A1A01077189 and NRF-2019M3F3A1A02071601).

## Conflict of Interest

The authors declare no conflict of interest.

## Keywords

all-optical neuromorphic devices, device structures, optoelectronic devices, synapses

Received: June 3, 2020

Revised: September 15, 2020

Published online: November 27, 2020

- [1] J. Von Neumann, *IEEE Ann. Hist. Comput.* **1993**, *15*, 27.
- [2] M. Komar, *Autom. Control. Comput. Sci.* **2017**, *51*, 701.
- [3] G. Indiveri, S.-C. Liu, *P. IEEE* **2015**, *103*, 1379.
- [4] G. Indiveri, B. Linares-Barranco, R. Legenstein, G. Deligeorgis, T. Prodromakis, *Nanotechnology* **2013**, *24*, 384010.
- [5] J. M. Montgomery, D. V. Madison, *Trends Neurosci.* **2004**, *27*, 744.
- [6] R. C. Atkinson, R. M. Shiffrin, *Psychol. Learn. Motiv.* **1968**, *2*, 89.
- [7] G. S. Snider, presented at 2008 *IEEE Int. Symp. Nano. Arch.*, Anaheim, June **2008**.
- [8] F. Yu, L. Q. Zhu, H. Xiao, W. T. Gao, Y. B. Guo, *Adv. Funct. Mater.* **2018**, *28*, 1804025.
- [9] J. T. Yang, C. Ge, J. Y. Du, H. Y. Huang, M. He, C. Wang, H. B. Lu, G. Z. Yang, K. J. Jin, *Adv. Mater.* **2018**, *30*, 1801548.
- [10] D. B. Strukov, G. S. Snider, D. R. Stewart, R. S. Williams, *Nature* **2008**, *453*, 80.
- [11] Z. Wang, S. Joshi, S. E. Savel'ev, H. Jiang, R. Midya, P. Lin, M. Hu, N. Ge, J. P. Strachan, Z. Li, *Nat. Mater.* **2017**, *16*, 101.
- [12] A. V. Avizienis, H. O. Sillin, C. Martin-Olmos, H. H. Shieh, M. Aono, A. Z. Stieg, J. K. Gimzewski, *PLoS One* **2012**, *7*, e42772.
- [13] F. Alibart, S. Pleutin, D. Guérin, C. Novembre, S. Lenfant, K. Lmimouni, C. Gamrat, D. Vuillaume, *Adv. Funct. Mater.* **2010**, *20*, 330.
- [14] J. Shi, S. D. Ha, Y. Zhou, F. Schoofs, S. Ramanathan, *Nat. Commun.* **2013**, *4*, 2676.
- [15] L. Q. Zhu, C. J. Wan, L. Q. Guo, Y. Shi, Q. Wan, *Nat. Commun.* **2014**, *5*, 3158.
- [16] Z.-D. Luo, X. Xia, M.-M. Yang, N. R. Wilson, A. Gruverman, M. Alexe, *ACS Nano* **2019**, *14*, 746.
- [17] X. Xie, J. Kang, Y. Gong, P. M. Ajayan, K. Banerjee, presented at *IEEE International Electron Devices Meeting*, **2017**.
- [18] M. Lee, W. Lee, S. Choi, J. W. Jo, J. Kim, S. K. Park, Y. H. Kim, *Adv. Mater.* **2017**, *29*, 1700951.
- [19] J. M. Shainline, S. M. Buckley, R. P. Mirin, S. W. Nam, *Phys. Rev. Appl.* **2017**, *7*, 034013.
- [20] Z. Cheng, C. Ríos, W. H. Pernice, C. D. Wright, H. Bhaskaran, *Sci. Adv.* **2017**, *3*, e1700160.
- [21] F. Zhou, Z. Zhou, J. Chen, T. H. Choy, J. Wang, N. Zhang, Z. Lin, S. Yu, J. Kang, H.-S. P. Wong, *Nat. Nanotechnol.* **2019**, *14*, 776.
- [22] S. Gao, G. Liu, H. Yang, C. Hu, Q. Chen, G. Gong, W. Xue, X. Yi, J. Shang, R.-W. Li, *ACS Nano* **2019**, *13*, 2634.
- [23] A. F. Benner, M. Ignatowski, J. A. Kash, D. M. Kuchta, M. B. Ritter, *IBM J. Res. Dev* **2005**, *49*, 755.
- [24] C. Sun, M. T. Wade, Y. Lee, J. S. Orcutt, L. Alloatti, M. S. Georgas, A. S. Waterman, J. M. Shainline, R. R. Avizienis, S. Lin, *Nature* **2015**, *528*, 534.

- [25] A. H. Atabaki, S. Moazeni, F. Pavanello, H. Gevorgyan, J. Notaros, L. Alloatti, M. T. Wade, C. Sun, S. A. Kruger, H. Meng, *Nature* **2018**, 556, 349.
- [26] S. Seo, S.-H. Jo, S. Kim, J. Shim, S. Oh, J.-H. Kim, K. Heo, J.-W. Choi, C. Choi, S. Oh, *Nat. Commun.* **2018**, 9, 5106.
- [27] L.-A. Kong, J. Sun, C. Qian, Y. Fu, J. Wang, J. Yang, Y. Gao, *Org. Electron.* **2017**, 47, 126.
- [28] Y. Fu, L.-A. Kong, Y. Chen, J. Wang, C. Qian, Y. Yuan, J. Sun, Y. Gao, Q. Wan, *ACS Appl. Mater. Interfaces* **2018**, 10, 26443.
- [29] R. A. John, J. Ko, M. R. Kulkarni, N. Tiwari, N. A. Chien, N. G. Ing, W. L. Leong, N. Mathews, *SMALL* **2017**, 13, 1701193.
- [30] M. Li, J. Yao, J. Azana, N. Zhu, presented at *14th International Conference On Optical Communications And Networks*, Nanjing, July **2015**.
- [31] M. Meyer, A. B. Abdallah, in *Photonic Interconnects For Computing Systems: Understanding And Pushing Design Challenges* (Eds: M. Nikdast, G. Nicolescu, S. L. Beux, J. Xu), River Publishers, Wharton **2017**, Ch. 10.
- [32] X.-Y. Xu, X.-L. Huang, Z.-M. Li, J. Gao, Z.-Q. Jiao, Y. Wang, R.-J. Ren, H. Zhang, X.-M. Jin, *Sci. Adv.* **2020**, 6, eaay5853.
- [33] S. Sun, V. K. Narayana, A. Mehrabian, T. El-Ghazawi, V. J. Sorger, arXiv. preprint. arXiv:1612.02486, **2016**.
- [34] D. Marpaung, J. Yao, J. Capmany, *Nat. Photonics* **2019**, 13, 80.
- [35] G. Agnus, W. Zhao, V. Derycke, A. Filoramo, Y. Lhuillier, S. Lenfant, D. Vuillaume, C. Gamrat, J. P. Bourgoin, *Adv. Mater.* **2010**, 22, 702.
- [36] L. Shao, H. Wang, Y. Yang, Y. He, Y. Tang, H. Fang, J. Zhao, H. Xiao, K. Liang, M. Wei, *ACS Appl. Mater. Interfaces* **2019**, 11, 12161.
- [37] S. Wang, X. Hou, L. Liu, J. Li, Y. Shan, S. Wu, D. W. Zhang, P. Zhou, *Research* **2019**, 2019, 1618798.
- [38] M. Zhang, Z. Fan, X. Jiang, H. Zhu, L. Chen, Y. Xia, J. Yin, X. Liu, Q. Sun, D. W. Zhang, *Nanophotonics* **2020**, 9, 2475.
- [39] T. Ahmed, S. Kuriakose, S. Abbas, M. J. Spencer, M. A. Rahman, M. Tahir, Y. Lu, P. Sonar, V. Bansal, M. Bhaskaran, *Adv. Funct. Mater.* **2019**, 29, 1901991.
- [40] S. Qin, F. Wang, Y. Liu, Q. Wan, X. Wang, Y. Xu, Y. Shi, X. Wang, R. Zhang, *2d Mater.* **2017**, 4, 035022.
- [41] J. Sun, S. Oh, Y. Choi, S. Seo, M. J. Oh, M. Lee, W. B. Lee, P. J. Yoo, J. H. Cho, J. H. Park, *Adv. Funct. Mater.* **2018**, 28, 1804397.
- [42] J. Yu, L. Liang, L. Hu, H. Duan, W. Wu, H. Zhang, J. Gao, F. Zhuge, T. Chang, H. Cao, *Nano Energy* **2019**, 62, 772.
- [43] L. Zhao, Z. Fan, S. Cheng, L. Hong, Y. Li, G. Tian, D. Chen, Z. Hou, M. Qin, M. Zeng, *Adv. Electron. Mater.* **2020**, 6, 1900858.
- [44] M. K. Kim, J. S. Lee, *Adv. Mater.* **2020**, 32, 1907826.
- [45] H. Tan, G. Liu, H. Yang, X. Yi, L. Pan, J. Shang, S. Long, M. Liu, Y. Wu, R.-W. Li, *ACS Nano* **2017**, 11, 11298.
- [46] H. Tan, G. Liu, X. Zhu, H. Yang, B. Chen, X. Chen, J. Shang, W. D. Lu, Y. Wu, R. W. Li, *Adv. Mater.* **2015**, 27, 2797.
- [47] C. Qian, S. Oh, Y. Choi, J.-H. Kim, J. Sun, H. Huang, J. Yang, Y. Gao, J.-H. Park, J. H. Cho, *Nano Energy* **2019**, 66, 104095.
- [48] S. Ham, S. Choi, H. Cho, S. I. Na, G. Wang, *Adv. Funct. Mater.* **2019**, 29, 1806646.
- [49] S. M. Kwon, S. W. Cho, M. Kim, J. S. Heo, Y. H. Kim, S. K. Park, *Adv. Mater.* **2019**, 31, 1906433.
- [50] M. K. Akbari, S. Zhuikov, *Nat. Commun.* **2019**, 10, 1.
- [51] S. W. Cho, S. M. Kwon, M. Lee, J.-W. Jo, J. S. Heo, Y.-H. Kim, H. K. Cho, S. K. Park, *Nano Energy* **2019**, 66, 104097.
- [52] M. Hu, C. E. Graves, C. Li, Y. Li, N. Ge, E. Montgomery, N. Davila, H. Jiang, R. S. Williams, J. J. Yang, *Adv. Mater.* **2018**, 30, 1705914.
- [53] H. Xu, J. Wu, Q. Feng, N. Mao, C. Wang, J. Zhang, *SMALL* **2014**, 10, 2300.
- [54] T. Vo-Dinh, J. Alarie, N. Isola, D. Landis, A. L. Wintenberg, M. Ericson, *Anal. Chem.* **1999**, 71, 358.
- [55] I. Nikitskiy, S. Goossens, D. Kufer, T. Lasanta, G. Navickaite, F. H. Koppens, G. Konstantatos, *Nat. Commun.* **2016**, 7, 11954.
- [56] L. Duan, L. Hou, T.-W. Lee, J. Qiao, D. Zhang, G. Dong, L. Wang, Y. Qiu, *J. Mater. Chem.* **2010**, 20, 6392.
- [57] X. Wang, H. Li, Y. Wu, Z. Xu, H. Fu, *J. Am. Chem. Soc.* **2014**, 136, 16602.
- [58] G. Liu, C. Wang, W. Zhang, L. Pan, C. Zhang, X. Yang, F. Fan, Y. Chen, R. W. Li, *Adv. Electron. Mater.* **2016**, 2, 1500298.
- [59] B. Kippelen, J.-L. Brédas, *Energy Environ. Sci.* **2009**, 2, 251.
- [60] J. Ji, J. H. Choi, *Adv. Mater. Interfaces* **2019**, 6, 1900637.
- [61] B. R. Lee, H. Choi, J. SunPark, H. J. Lee, S. O. Kim, J. Y. Kim, M. H. Song, *J. Mater. Chem.* **2011**, 21, 2051.
- [62] N. Munzenrieder, K. H. Cherenack, G. Troster, *IEEE Trans. Electron Devices* **2011**, 58, 2041.
- [63] J. Yao, N. Xu, S. Deng, J. Chen, J. She, H.-P. D. Shieh, P.-T. Liu, Y.-P. Huang, *IEEE Trans. Electron Devices* **2011**, 58, 1121.
- [64] H.-K. Noh, K.-J. Chang, B. Ryu, W.-J. Lee, *Phys. Rev. B* **2011**, 84, 115205.
- [65] O. Malinkiewicz, A. Yella, Y. H. Lee, G. M. Espallargas, M. Graetzel, M. K. Nazeeruddin, H. J. Bolink, *Nat. Photonics* **2014**, 8, 128.
- [66] Y. H. Kim, H. Cho, J. H. Heo, T. S. Kim, N. Myoung, C. L. Lee, S. H. Im, T. W. Lee, *Adv. Mater.* **2015**, 27, 1248.
- [67] D. Panda, T.-Y. Tseng, *J. Mater. Sci* **2013**, 48, 6849.
- [68] Y. S. Zhao, H. Fu, A. Peng, Y. Ma, Q. Liao, J. Yao, *Acc. Chem. Res.* **2010**, 43, 409.
- [69] F. Ghasemi, *Sci. Rep.* **2020**, 10, 14786.
- [70] C. Choi, M. K. Choi, S. Liu, M. S. Kim, O. K. Park, C. Im, J. Kim, X. Qin, G. J. Lee, K. W. Cho, *Nat. Commun.* **2017**, 8, 15684.
- [71] J. Tersoff, *Phys. Rev. Lett.* **1984**, 52, 465.
- [72] N. Yang, C.-Z. Hu, Z.-Q. Ren, S.-Y. Bao, B.-B. Tian, F.-Y. Yue, P.-H. Xiang, N. Zhong, C.-G. Duan, J.-H. Chu, *ACS Appl. Electron. Mater.* **2020**, 2, 1035.
- [73] M. Lenzlinger, E. Snow, *J. Appl. Phys.* **1969**, 40, 278.
- [74] X. Zhu, W. D. Lu, *ACS Nano* **2018**, 12, 1242.
- [75] Y. Wang, Z. Lv, J. Chen, Z. Wang, Y. Zhou, L. Zhou, X. Chen, S. T. Han, *Adv. Mater.* **2018**, 30, 1802883.
- [76] C. Yang, J. Qian, S. Jiang, H. Wang, Q. Wang, Q. Wan, P. K. L. Chan, Y. Shi, Y. Li, *Adv. Opt. Mater.* **2020**, 8, 2000153.
- [77] L. Yin, W. Huang, R. Xiao, W. Peng, Y. Zhu, Y. Zhang, X. Pi, D. Yang, *Nano Lett.* **2020**.
- [78] D. Hao, J. Zhang, S. Dai, J. Zhang, J. Huang, *ACS Appl. Mater. Interfaces* **2020**, 12, 39487.
- [79] B. Pradhan, S. Das, J. Li, F. Chowdhury, J. Cherusseri, D. Pandey, D. Dev, A. Krishnaprasad, E. Barrios, A. Towers, *Sci. Adv.* **2020**, 6, eaay5225.
- [80] Y. C. Chiang, C. C. Hung, Y. C. Lin, Y. C. Chiu, T. Isono, T. Satoh, W. C. Chen, *Adv. Mater.* **2020**, 2002638.
- [81] W. Deng, X. Zhang, R. Jia, L. Huang, X. Zhang, J. Jie, *NPG Asia Mater.* **2019**, 11, 1.
- [82] S. Dai, X. Wu, D. Liu, Y. Chu, K. Wang, B. Yang, J. Huang, *ACS Appl. Mater. Interfaces* **2018**, 10, 21472.
- [83] H. K. He, R. Yang, W. Zhou, H. M. Huang, J. Xiong, L. Gan, T. Y. Zhai, X. Guo, *SMALL* **2018**, 14, 1800079.
- [84] M. Kumar, S. Abbas, J. Kim, *ACS Appl. Mater. Interfaces* **2018**, 10, 34370.
- [85] Z. Xu, Y. Yu, S. Arya, I. A. Niaz, Y. Chen, Y. Lei, M. A. R. Miah, J. Zhou, A. C. Zhang, L. Yan, *Nano Lett.* **2020**, 20, 2144.
- [86] A. Bera, H. Peng, J. Lourembam, Y. Shen, X. W. Sun, T. Wu, *Adv. Funct. Mater.* **2013**, 23, 4977.
- [87] P. Wang, M. E. Nasir, A. V. Krasavin, W. Dickson, A. V. Zayats, *Nano Lett.* **2020**, 20, 1536.
- [88] D.-C. Hu, R. Yang, L. Jiang, X. Guo, *ACS Appl. Mater. Interfaces* **2018**, 10, 6463.

- [89] Y. Ren, L. Hu, J.-Y. Mao, J. Yuan, Y.-J. Zeng, S. Ruan, J.-Q. Yang, L. Zhou, Y. Zhou, S.-T. Han, *J. Mater. Chem.* **2018**, *6*, 9383.
- [90] A. H. Jaafar, N. Kemp, *Carbon* **2019**, *153*, 81.
- [91] C. Ríos, M. Stegmaier, P. Hosseini, D. Wang, T. Scherer, C. Wright, H. Bhaskaran, W. Pernice, *Nat. Photonics*, **2015**, *9*, 725.
- [92] J. Feldmann, N. Youngblood, C. D. Wright, H. Bhaskaran, W. Pernice, *Nature* **2019**, *569*, 208.
- [93] H. Altug, D. Englund, J. Vučković, *Nat. Phys.* **2006**, *2*, 484.
- [94] S. Wu, S. Buckley, J. R. Schaibley, L. Feng, J. Yan, D. G. Mandrus, F. Hatami, W. Yao, J. Vučković, A. Majumdar, *Nature* **2015**, *520*, 69.
- [95] B. Ellis, M. A. Mayer, G. Shambat, T. Sarmiento, J. Harris, E. E. Haller, J. Vučković, *Nat. Photonics* **2011**, *5*, 297.
- [96] B.-S. Song, S. Noda, T. Asano, Y. Akahane, *Nat. Mater.* **2005**, *4*, 207.
- [97] R. E. Evans, M. K. Bhaskar, D. D. Sukachev, C. T. Nguyen, A. Sipahigil, M. J. Burek, B. Machielse, G. H. Zhang, A. S. Zibrov, E. Bielejec, *Science* **2018**, *362*, 662.
- [98] K. Liu, N. Li, D. K. Sadana, V. J. Sorger, *ACS Photonics* **2016**, *3*, 233.
- [99] Y. Zhu, X. Hu, H. Yang, Q. Gong, *Sci. Rep.* **2014**, *4*, 3752.
- [100] K. Nozaki, T. Tanabe, A. Shinya, S. Matsuo, T. Sato, H. Taniyama, M. Notomi, *Nat. Photonics* **2010**, *4*, 477.
- [101] M. Takiguchi, N. Takemura, K. Tateno, K. Nozaki, S. Sasaki, S. Sergent, E. Kuramochi, T. Wasawo, A. Yokoo, A. Shinya, *ACS Photonics* **2020**, *7*, 1016.
- [102] T. Tanabe, M. Notomi, S. Mitsugi, A. Shinya, E. Kuramochi, *Opt. Lett.* **2005**, *30*, 2575.
- [103] P. Lalanne, C. Sauvan, J. P. Hugonin, *Laser Photonics Rev.* **2008**, *2*, 514.
- [104] Y. Akahane, T. Asano, B.-S. Song, S. Noda, *Nature* **2003**, *425*, 944.
- [105] E. Kuramochi, M. Notomi, S. Mitsugi, A. Shinya, T. Tanabe, T. Watanabe, *Appl. Phys. Lett.* **2006**, *88*, 041112.
- [106] K. Nozaki, A. Shinya, S. Matsuo, Y. Suzaki, T. Segawa, T. Sato, Y. Kawaguchi, R. Takahashi, M. Notomi, *Nat. Photonics* **2012**, *6*, 248.
- [107] M. Sheik-Bahae, A. A. Said, T.-H. Wei, D. J. Hagan, E. W. Van Stryland, *IEEE J. Quantum Electron.* **1990**, *26*, 760.
- [108] E. Kuramochi, K. Nozaki, A. Shinya, K. Takeda, T. Sato, S. Matsuo, H. Taniyama, H. Sumikura, M. Notomi, *Nat. Photonics* **2014**, *8*, 474.
- [109] H. Tan, Q. Tao, I. Pande, S. Majumdar, F. Liu, Y. Zhou, P. O. Persson, J. Rosen, S. van Dijken, *Nat. Commun.* **2020**, *11*, 1369.
- [110] Y. Lee, J. Y. Oh, W. Xu, O. Kim, T. R. Kim, J. Kang, Y. Kim, D. Son, J. B.-H. Tok, M. J. Park, *Sci. Adv.* **2018**, *4*, eaat7387.
- [111] M. Kumar, J. Kim, C.-P. Wong, *Nano Energy* **2019**, *63*, 103843.
- [112] T. Ahmed, S. Kuriakose, E. L. Mayes, R. Ramanathan, V. Bansal, M. Bhaskaran, S. Sriram, S. Walia, *Small* **2019**, *15*, 1900966.
- [113] R. A. John, F. Liu, N. A. Chien, M. R. Kulkarni, C. Zhu, Q. Fu, A. Basu, Z. Liu, N. Mathews, *Adv. Mater.* **2018**, *30*, 1800220.



**Seungho Song** is currently a graduate student in the School of Advanced Materials Science and Engineering, Sungkyunkwan University, Suwon, Korea. He received his B.S degree from the School of Advanced Materials Science and Engineering, Sungkyunkwan University, Suwon, Korea. His current areas of research interest include metal oxides, flexible thin-film transistor devices, and optoelectronic neuromorphic devices.



**Jeehoon Kim** is currently a graduate student in the School of Advanced Materials Science and Engineering, Sungkyunkwan University, Suwon, Korea. He received his B.S. degree in the Department of Advanced Material Engineering, Chungbuk National University, Cheongju, Korea. His current areas of research interest include metal oxides, flexible thin-film transistors, and optoelectronic neuromorphic devices.



**Sung Min Kwon** received his M.S. degree from the School of Electrical and Electronics Engineering at Chung-Ang University. He continued to be a Ph.D. student in the School of Electrical and Electronics Engineering at Chung-Ang University. His research interests are focused on display, advanced memory, and optoelectronic devices based on metal oxides, metal chalcogenides, and quantum dot materials.



**Jeong-Wan Jo** is a postdoctoral researcher in the Department of Engineering at the University of Cambridge. He received a Ph.D. from the School of Electrical and Electronics Engineering of Chung-Ang University in 2019. His current research interests are focused on low-temperature solution-processed flexible and stretchable metal-oxide TFTs and their application in various electronic devices.



**Sung Kyu Park** is the Professor of School of Electrical and Electronics Engineering at Chung-Ang University, Seoul, Korea. He received his Ph.D. degree from The Pennsylvania State University, University Park, PA in 2007. He was employed at Korea Electronics Technology Institute and Eastman Kodak Company, Rochester, NY. Prof. Park's research focuses on exploratory electronic materials and devices. His current areas of research interest include quantum dots, organic, metal-oxide, chalcogenide materials based electronic devices and systems for ultra-fine fiber-based electronics, wearable sensors, neuromorphic systems, and display technology.



**Yong-Hoon Kim** is an associate professor in the School of Advanced Materials Science and Engineering, Sungkyunkwan University, Suwon, Korea. He received his Ph.D. from Seoul National University, Seoul, Korea. At Sungkyunkwan University, his research focuses on developing flexible electronic devices including flexible displays and wearable sensors. His current research includes textile-based wearable electronics, low-temperature oxide-based devices, and neuromorphic devices.